JPRS-CST-92-015
29 JULY 1992

FOREIGN BROADCAST INFORMATION SERVICE

JPRS Report

Science & Technology

China

HIGH-POWER LASER AND PARTICLE BEAMS

JPRS-CST-92-015
29 JULY 1992

SCIENCE & TECHNOLOGY

CHINA

HIGH-POWER LASER AND PARTICLE BEAMS

CONTENTS

Experimental Research on 1.5 GHz RF Superconducting Niobium Cavity

92FE0442A Chengdu QIANG JIGUANG YU LIZI SHU [HIGH POWER LASER AND PARTICLE BEAMS] in Chinese Vol 4 No 1, Feb 92 pp 15-32

[Article by Zhao Kui [6392 5688], Wang Guangwei [3769 0342 0251], Wang Lifang [3769 5461 5364], and Chen Jiaer [7115 0163 3167] of the Institute of Heavy Ion Physics, Beijing University, P.O. Box 100871, and Zhang Baocheng [1728 0202 3397] and Song Jinhu [1345 6651 5706], Department of Technical Physics, Beijing University, P.O. Box 100871: "Experimental Research on 1.5 GHz RF Superconducting Niobium Cavity"; MS received 21 Aug 91, revised 30 Oct 91, supported by the National High-Tech Laser Technology Fund]

[Text] **Abstract**

Research on an RF superconducting cavity at Beijing began in 1988. After three years of hard work, substantial progress has been obtained, and has been well recognized by experts worldwide. The preparation and procedures for the low-temperature superconducting experiment are described in detail. The paper also summarizes progress and accomplishments in RF (radio-frequency) superconducting experimental technique, microwave and phase-locked measurement, post-purification of cavity, computer simulation design and computer control, and data acquisition and processing. Presently, an accelerating gradient of 8.6 MV/m ($Q_0 = 6.5 \times 10^8$) has been obtained in a 1.5 GHz niobium cavity operating in the CW mode. At 2 K, it was measured that $Q_0 = 8 \times 10^9$. These experimental results are at the cutting edge in the international field.

I. Introduction

RF superconducting technology has been used in accelerators for some time. In 1965, a lead-plated superconducting cavity was developed at Stanford University to accelerate electrons. After more than two decades of effort, substantial progress has been made to improve the shape, material performance and accelerating gradient of superconducting cavities.[1] Presently, more than 20 laboratories worldwide are using or building high-energy superconducting accelerators for heavy ions and electrons.

The characteristics of a superconducting cavity include high gradient, large beam diameter, capability of operating in the CW mode, and low operating

frequency.[2] There are advantages in using a superconducting cavity in a high-energy intense electron beam (e-beam) accelerator. A superconducting accelerator is particularly appropriate for a free electron laser (FEL) because it has very stringent requirements for beam quality, intensity, and mean power. In the late 80's, a scheme for using a superconducting cavity and an optical cathode high-intensity injector was presented with the objective of increasing the brightness of an FEL or TEV linear collider.[3]

Today's superconducting cavity has excellent RF characteristics. In the laboratory, a single cavity has an accelerating gradient of 25 MV/m ($Q_0 \approx 10^9$). Based on BCS theory, the accelerating gradient of a pure niobium (Nb) cavity can be as high as 50 MV/m.[1] The experimental value is still far less than that value. Through a large number of experiments and continuous investigation, it is recognized that the surface characteristics of the superconducting cavity are critical to its overall performance. Processes such as multiple e-beam smelting, increasing RRR (residual resistance ratio), chemical washing, high-temperature treatment in ultrahigh vacuum, and artificial oxide-film formation can effectively improve its performance. Nevertheless, field-effect emission is still the limiting factor preventing the acceleration gradient from rising further. Some large laboratories (e.g., KEK, DESY, CERN, and Cornell) are looking for new methods and techniques to modify the cavity surface in order to find a breakthrough in acceleration gradient.[4,5,6,7]

The heavy-ion superconducting cavity group at Beijing University has done a great deal of work on post-treatment of the cavity to raise the acceleration gradient. As a result, a series of effective measures has been established. Substantial progress has been made in a relatively short period of time. We have measured a gradient of 8.6 MV/m (in CW mode). At 2 K, a cavity quality factor of 8×10^9 has been obtained. This paper presents methods and techniques used to improve [the quality factor] Q and the acceleration gradient E_{acc}.

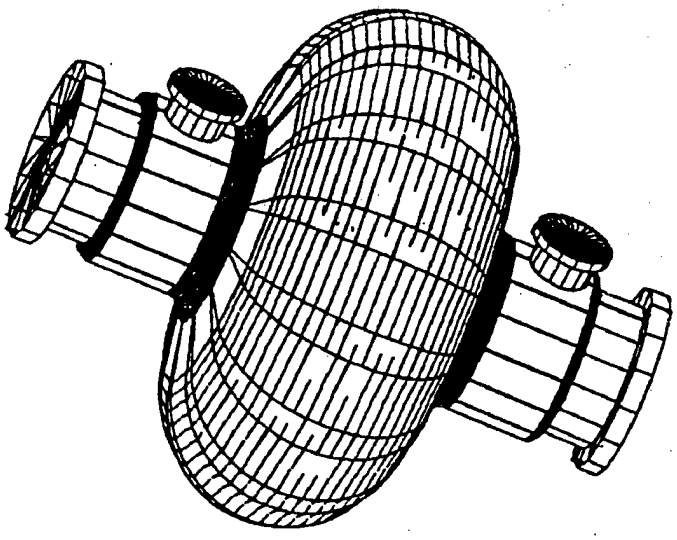

Figure 1. Elliptical Cavity

II. Design Analysis and PC-Based Program

1. Design Analysis

When an Nb cavity is running in a superconducting state, its resistance (R_s) is of the order of nΩ. It is approximately 5 orders of magnitude lower than the R_s of a copper cavity at liquid-nitrogen temperature.[1] This extremely low resistance is a unique feature for Nb. An important point is that the shape of the superconducting cavity has very little impact on the RF power conversion

efficiency. Hence, cavity design should address other issues such as effects due to dark arc and higher-order modes (HOMs). Figure 1 shows an elliptical superconducting cavity. The beam tube has coupling openings and both ends have cutoff waveguides. A portion of the accelerating gradient has a transitional circular arc and it also has a large-aperture beam tube to effectively suppress the dark-arc effect and beam-induced field. The base mode, HOMs, and wake-field effects of a 1.5 GHz LE-type elliptical single harmonic cavity (β=1) have been analyzed using programs such as SUPERFISH, URMELT, and TBCI. Relevant results have been published elsewhere.[10,11,12] Figure 2 shows the wake field caused by a single focused pulse. An HP 8753C network analyzer was used to measure all the modes below 3.0 GHz associated with a 1.5 GHz Nb cavity at room temperature; the results are essentially consistent with the computer analysis. Table 1 is a comparison of measured and calculated values.

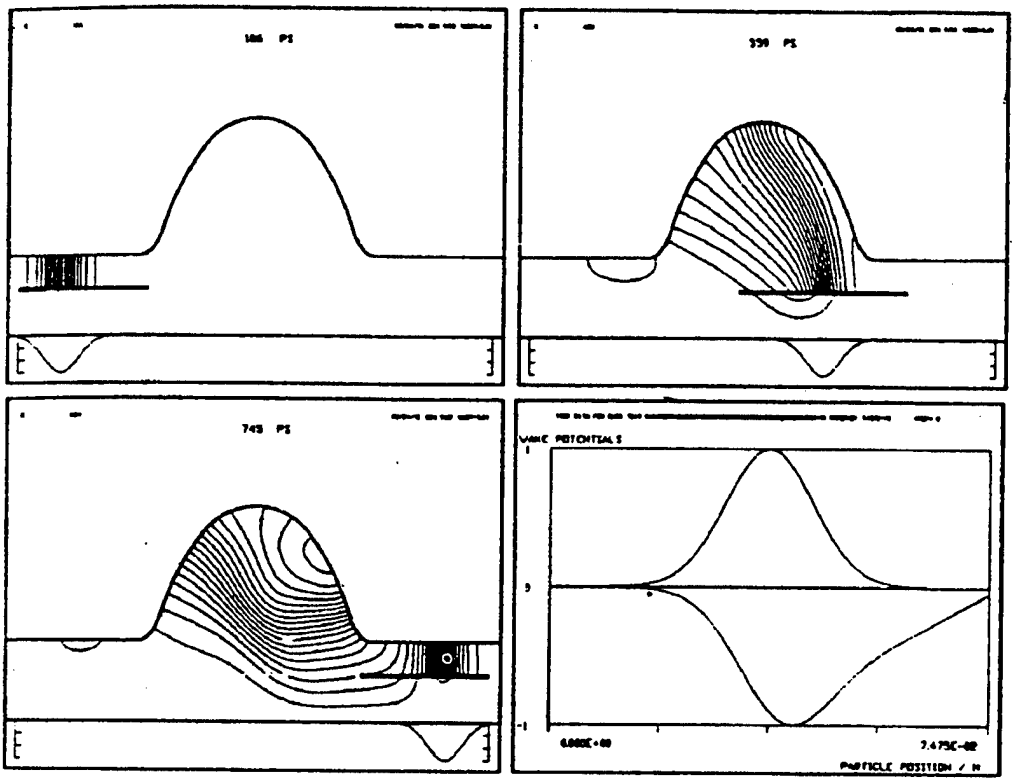

Figure 2. Wake Field Simulation of Elliptical Cavity

Table 1. Comparison Between Measurement and Computation

MODE	URMELT (MHz)	Meas. (MHz)	MODE	URMELT (MHz)	Meas. (MHz)
TM010	1470.22	1467.70	TM110	2058.45	2043.54
TM011	2792.13	2800.40	TM111	2621.95	2585.17
TM020	2977.62	2975.84	TM112	2955.58	2974.58
TE111	1889.80	1868.32			

2. Running Software Programs on PC

In computer design analysis, an outstanding accomplishment was achieved. Programs such as URMELT and TBCI have been successfully transplanted onto a 386-PC. To run a large program on a PC, the first issue is to solve the internal memory problem. The code and data segment of programs such as URMELT and TBCI are much larger than 640 K, which makes it impossible to run directly in a DOS environment. In the past, the conventional method has been to use overlays for the code and to open temporary files for the large data segment. However, this requires the careful analysis of each module and every executable statement in the source code. It takes an incredible amount of work.

Our approach is to use virtual memory; this divides up a portion of the hard drive for virtual memory. When a 386-PC operates under a protected virtual address mode, it is capable of managing 16 M of real memory and 64 T (T = M x M) of virtual memory. This makes it possible to run large programs on a PC. In this case, the size of the program is determined by the capacity of the hard drive. On our HP-312 PC, with 10 M internal memory (2 M real and 8 M virtual), both URMELT and TBCI could be run normally. The speed is approximately one-third to one-half of that on the VAX. However, with multiuser time-sharing on a VAX, it is comparable in speed. Figure 2 shows some TBCI results obtained from the HP-312 PC.

The fact that these programs can run on a 386-PC is extremely convenient for the research group, not only saving us time but also money.

III. Cryostat and Ultrahigh-Vacuum System

1. Cryostat

The 1.5 GHz Nb superconducting cavity experiment has to be performed at 2~4.2 K. To this end, a cryostat was constructed. After two years of effort, we completed the fabrication and installation of a system consisting of a large cryostat, a 100-liter liquid helium (He) Dewar, two 100-liter liquid-nitrogen (N_2) Dewars, a liquid-He duct, an He recovery duct and gauges for temperature and liquid-He height. The construction of this apparatus ensures the smooth execution of superconductivity experiments.

The 100-liter cryostat is the major equipment required to perform the experiment. The development of such a large low-temperature liquid-He device had never been reported domestically. Due to lack of information, the initial design was sent to DESY (Germany) for review by foreign experts. Our German colleagues came back with 10 major modifications. The design was then revised and made simpler and more practical. The new design stresses safety and the ultrahigh-vacuum requirement associated with the Nb superconducting cavity. Figure 3 is a sketch of the cryostat, which is approximately 175 cm high with a maximum outer diameter of 75 cm. The Nb cavity and the cryostat are on two separate vacuum systems. The cryostat uses a high-speed molecular pump and the system is required to provide 10^{-4}~10^{-5} Pa of vacuum. The Nb superconducting cavity has an ultrahigh-vacuum system.

After about a year of operation, the entire cryostat system has essentially met the design requirements. Liquid He in the cryostat evaporates at a rate of 1 percent per hour. The 100-liter liquid-He Dewar evaporates at a rate of less than 1.5 percent per day.

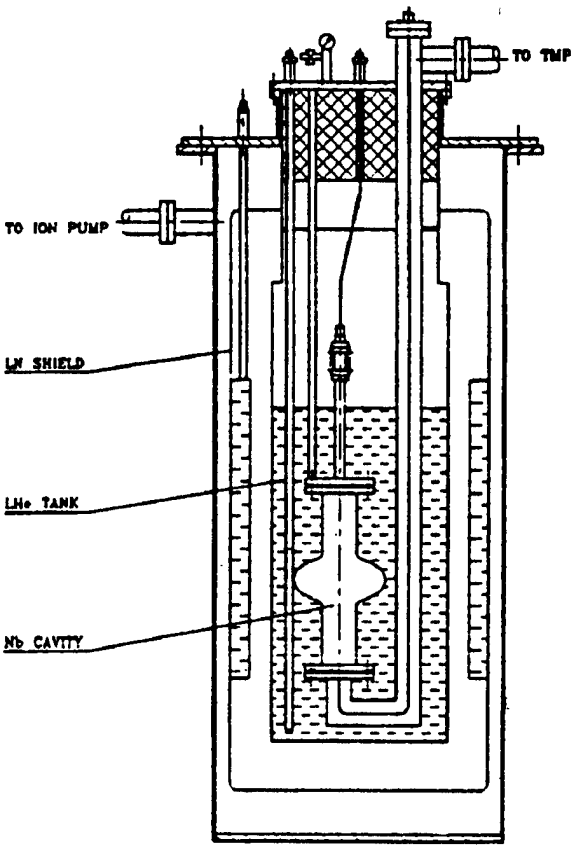

Figure 3. Liquid-He Cryostat

2. Ultrahigh-Vacuum System

The internal surface of the superconducting cavity must be extremely clean. Otherwise, it has a significant impact on Q and E_{acc}. The 1.5 GHz Nb cavity is vertically mounted in the cryostat and is connected to the vacuum line in an overhead manner to prevent any debris from falling into the cavity. Both ends of the cavity are sealed with an indium (In) sealing surface. The inner diameter of the In seal flange must be designed according to the actual size of the beam pipe flange. It must be highly accurate. The diameter of the sealing In wire is 1 mm. These two large-aperture sealed connections can directly influence the ultrahigh-vacuum achievable by the system. Especially when liquid He is in a superfluid state, these connections are the weak links. Two cryostatic absorption pumps and an ion pump provide an oil-free pumping system for the Nb cavity. The entire system is metal-sealed with ultrahigh-vacuum metal valves. The RF feed-throughs are 50-Ω ceramic-seal coaxial connectors (total 99). An ultrahigh-vacuum jewel valve is installed at the end of the vacuum line as a control valve for helium treatment experiments.

This system can reach 10^{-6}~10^{-7}Pa of vacuum before using liquid N_2 to lower the temperature. After adding liquid N_2 and He, it can reach 10^{-8}Pa. After repeated tests with liquid He, the system was found to be reliable for low-temperature physical experiments. The first phase of work was thus completed smoothly.

3. Low-Pressure, Low-Temperature Experiment

The Q value of a superconducting cavity varies with temperature.[1] At 4.2 K, Q is (2~4) x 10^8 for the 1.5 GHz Nb cavity. At 2 K, Q_0 = (6~9) x 10^9. Hence, it is essential to achieve an ultralow temperature in order to reach a higher gradient. In order to reach an ultralow temperature, we employed a method to lower temperature and reduce pressure by a mechanical pump. After many tests, 2 K was finally achieved in the 100-liter cryostat and Q_0 measured 8 x 10^9. At 2.12 K, liquid He is a superfluid, posing a serious challenge to the vacuum components in the liquid-He tank because superfluid He is extremely permeable.

After numerous low-temperature, low-pressure experiments, the vacuum inside the Nb cavity remained unchanged. This demonstrates the integrity of the In seals and other metal seals. It is rare in China for such a large liquid-He vessel to reach such a low temperature.

4. Shielding of the Earth's Magnetic Field

The Earth's magnetic field has a great deal of impact on the RF characteristics of the superconducting cavity. Hence, it is necessary to establish a magnetic shield around the Nb cavity. We added several layers of thin film of a high-μ material, which is an amorphous metal (Fe-Ni-Si-B); the thin ribbon is 0.04 mm x 100 mm (thickness x width), total weight 6 kg. The axial and horizontal magnetic field inside the cryostat were measured by technicians from the Department of Geophysics at Beijing University using a model DM 2220 Digital Magnetometer (U.S.-made). It was found that the axial magnetic field is one-seventh and the horizontal magnetic field is one-twentieth of the Earth's magnetic field. This essentially satisfies the requirement for the superconducting experiment.

IV. Post-Treatment of Nb Cavity

After a superconducting Nb cavity is machined and welded, it needs to be polished mechanically, electrically, and chemically and then purified after putting on a titanium (Ti) film. As a result of these processes, a high-quality, high-thermal-conductivity inner surface is produced. These processes help improve the quality factor Q and accelerating gradient E_{acc}. This involves materials science, chemistry and thermal treatment. In order to obtain the ideal RF superconducting conditions, the following work was done.

1. Analysis of Nb Material

The superconducting cavity inside an electron accelerator is usually made of high-purity thin Nb plate. Commercial-grade Nb cannot be used directly; several times of e-beam smelting are required to raise its purity. After raising purity, it is necessary to improve its thermal conductivity. The normal method is to evaporate a Ti coating on the Nb surface in order to remove the impurity in Nb by way of the combining process.

We analyzed and compared the high-RRR Nb supplied by DESY to the e-beam-smelted Nb processed by the Institute of Nonferrous Metals. Table 2 shows the semiquantitative chemical composition of the two specimens. Sample #1 is from DESY and is not very impressive from the standpoint of impurity. Figure 4, an electron spectrum of the specimen, shows that the surface is covered by a layer of Nb_2O_5 several hundred angstroms in thickness. After repeated RF superconducting experiments, it was verified that this oxide layer could stabilize the RF characteristics of the cavity. Presently, this high-quality oxide film is being added to the purification process at KEK and CEBAF as well.

Table 2. Semi-Quantitative Chemical Analysis of Two Nb Specimens
Sample #1 [Figures in percent]

Ni	Zr	Rh	Sn	Tl	Ta	Mg	Pt	Ti
0.001	0.003~ 0.01	0.01	0.001	0.001	0.1	0.001	0.002	0.001~ 0.01

Sample #2 [Figures in percent]

Hf	Zr	Tl	Al	Pt	Cu	Ti
0.01	0.003	0.001	0.003	0.001	0.001	0.003

2. Chemical Polishing

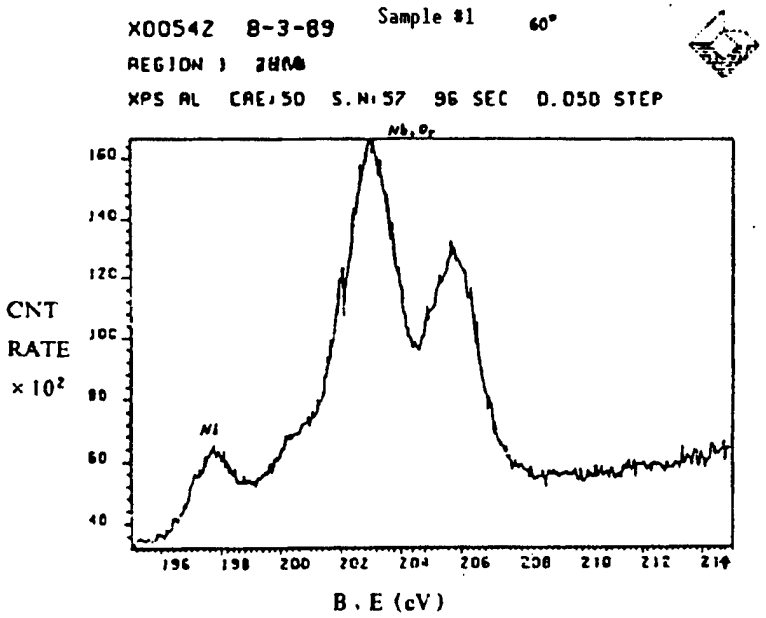

Figure 4. Photoelectron Spectrum of Nb Surface

The 1.5 GHz Nb cavity manufactured by Dornier Corporation is made of high-purity Nb with RRR = 300. Usually, the thermal breakdown threshold is higher when RRR is high. It will be easier to attain a higher accelerating gradient E_{acc}; however, it is more difficult to chemically clean this high-RRR Nb. In the acid washing process, it is easy to incorporate H^+ or phosphate into the Nb surface to cause substantial deterioration of surface characteristics. In order to avoid this situation, we conducted numerous chemical polishing experiments and finally established an effective polishing method.

Chemical polishing was done according to the method used at DESY and KEK.[13] Figure 5 [photos not reproduced] shows scanning electron micrographs of a specimen before and after chemical polishing. It is obvious from the pictures that the crystals are well aligned on the Nb surface after chemical polishing. The polishing solution is composed of a fixed ratio of HF (40%), HNO_3 (65%), and H_3PO_4 (85%). The number of washes and the time of exposure must be carefully controlled. The Nb cavity needs to be cooled during the process. Cleaning after acid polishing is very critical. The resistivity of the deionized water used must be monitored frequently; especially in the final rinse, it should be at approximately 18 MΩ. The cavity is mounted on a special support during acid polishing. It can be rotated to allow the acid to come

into contact with the cavity wall evenly and to make the discharge of the solution easier. Acid-resistant flanges and valves are used on both sides of the beam pipe. The first chemical polishing prior to thermal treatment must remove a surface layer 20~30 μ in thickness. After thermal treatment, it needs to be chemically polished one more time to remove another 5~10 μ.

3. High-Temperature Treatment

We began conducting RF superconducting experiments in October 1990. In the first two experiments, only chemical polishing was done and the results were not satisfactory. After reviewing the data obtained in KEK, DESY, and Cornell, our preliminary conclusion was that stress in the cavity had to be relieved. This stress comes from machining and welding. According to a 1989 Cornell publication, it was reported that the Q_0 for their 1.5 GHz Nb cavity was two orders of magnitude lower than the expected value and could not be improved until the stress was relieved by heat treatment. DESY also presented the same issue in a 1989 meeting. In reference to their experience, a thermal treatment procedure was formulated as follows: The heat-resistant is done in a vacuum furnace with a vacuum better than 1×10^{-3}Pa and at a temperature of 850~900°C for one hour. The vacuum pumps should not be turned off during cooling. The Nb cavity is placed in a Ti box during the heat treatment. Impurities in Nb are evaporated from the surface at high temperature and may be readsorbed during cooling. With a Ti box, impurity ions are easily adsorbed by Ti to keep the Nb cavity from secondary contamination.

The Nb cavity used in our third liquid-He-temperature experiment was thermally treated; this is the very cavity with which we had a major breakthrough. The measured Q_0 was of the order of 10^8 (at 4.2 K). With reduced pressure and lower temperature, Q_0 was found to be of the order of 10^9. These numbers are consistent with results reported in other countries and they are also in agreement with theoretical values. Furthermore, we also noticed that the heat-treated cavity was very reproducible. We did not see Q_0 drop due to temperature excursion.[15,16]

4. Ultraclean Installation

In order to prevent contamination, the cleaned cavity must be installed in an ultraclean environment. After chemical polishing, the cavity is filled with ultrapure water to prevent any impurity from entering the cavity. It is then immediately sent to an ultraclean room for installation. Prior to installation, the cavity is rinsed again with ultrapure water. The ultraclean room is equipped with an air curtain and air filters. It also has a Class-100 workbench for two to ensure that there are fewer than 100 dust particles more than 0.5 μm in size per cubic foot over the workbench. The number of such dust particles in a cubic foot of normal air is 210,000. When installing the main coupler, pure nitrogen evaporated from the liquid-nitrogen Dewar is fed into the cavity through the heating tube to create a positive pressure inside the cavity. This is to prevent air from coming in contact with the cavity surface to minimize the chance of any impurities entering the cavity. After the cavity is connected to the main coupler, nitrogen is injected from the main coupler.

These two components are then connected to the vacuum system. During this process, a positive pressure is always maintained inside the cavity.

After turning on the ion pump, the entire system is baked for approximately 20 hours, and will reach the desired vacuum in a week or so.

V. Microwave and Phase-Locked Measurement Technique

Microwave measurement is a key step in RF superconducting experiments. Under superconducting conditions, the resistance R_s of the 1.5 GHz Nb cavity is less than a few hundred ohms, which is five orders of magnitude lower than the R_s of a copper cavity. Hence, the quality factor of the superconducting cavity is as high as 10^8~10^9. The half-power bandwidth of its resonant curve is only a few Hertz wide and the field-decay time constant is 30~300 ms. These properties make the measurement of RF parameters and search for the resonant point very difficult. From the very beginning, we recognized that microwave measurements involving such a high-Q superconducting cavity were never attempted in China and it would require the appropriate test methods and instrumentation with high accuracy and stability.

1. Instrument Setup

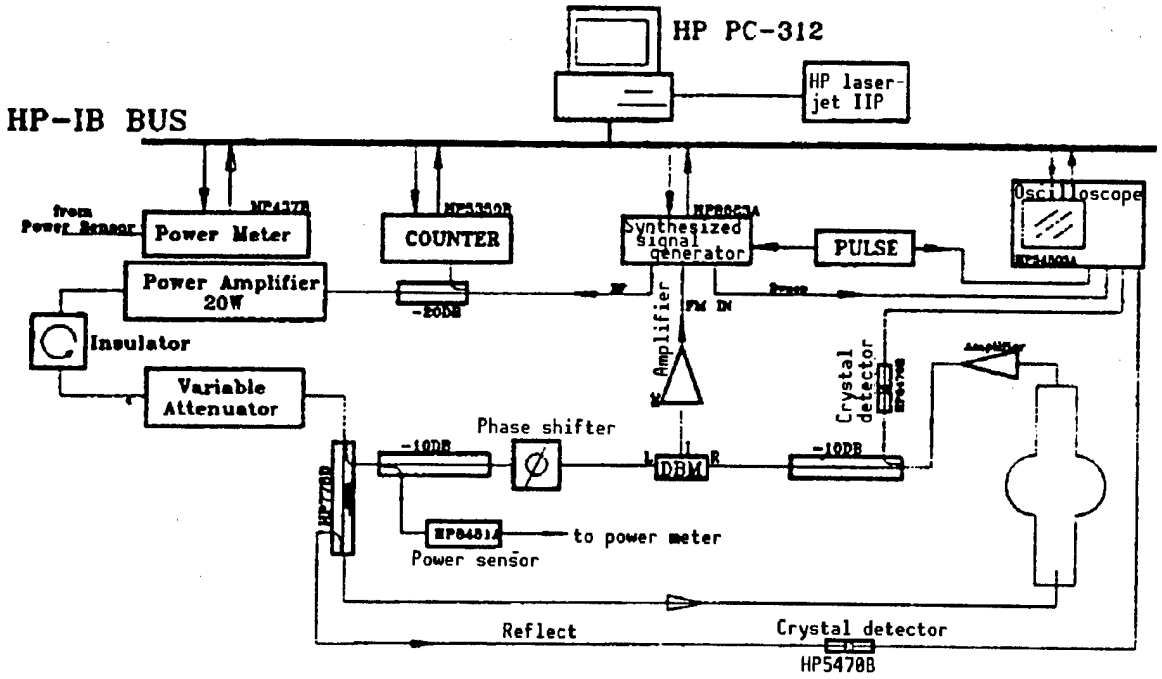

Figure 6. Microwave Phase-Locked Loop

Figure 6 shows the microwave measurement circuit used in the low-temperature superconducting experiment, and essentially shows our instrument setup as well. The synthesized signal generator is an HP 8663A, which has a frequency stability of 10^{-10}/day. The output signal has a resolution of 0.4 Hz at near 1.5 GHz, which is less than the half-power bandwidth of the superconducting cavity. The signal generator is capable of scanning and phase-locked tuning.

When searching for the superconducting point by frequency scanning, a signal generator must have the kind of high resolution and stability as those described above.

The bandwidth of the four-channel digital oscilloscope, an HP 54503A, is DC-500 MHz. The horizontal time axis has 501 points. (The HP-IB remote data acquisition system has 1,024 points). The vertical voltage axis is eight-bit. Its accuracy is $1/2^8 = 0.4$ percent. (The HP-IB remote data acquisition system is 16-bit with an accuracy of 1.5×10^{-5}.) It can automatically detect the maximum and minimum signal. Furthermore, it is capable of measuring the voltage at a specific time by remote control. It also can determine the time at which the signal is at a specific voltage. The oscilloscope also has memory for storage.

The power meter is an HP 437B and its measurement range is: 100 kHz~50 GHz in frequency, -70 dBm to +44 dBm in power, and 0.1 percent in accuracy. The frequency counter is an HP 5350B. It has an accuracy of 1 Hz near 1.5 GHz and the gate is 200 ms wide.

The HP PC-312 controller has two CPUs. It not only can function as a 386 microcomputer but also can be connected to the signal generator, oscilloscope, power meter, frequency counter, and laser printer through an IEEE-488.2 interface to form a fully automated data acquisition, processing, storage, and print-out system.

The 20-W RF solid-state amplifier is the final-stage power amplifier of the measurement system. It was constructed by Institute 54 of the Ministry of Machine-Building and Electronics Industry (MMEI). The frequency range of the amplifier is 1.4 GHz~1.6 GHz. When Q_0 of the Nb cavity is of the order of 10^9, the maximum power output meets the experimental requirement.

The system employs directional couplers such as HP 778D (20 dB), Narda 4242-20 and TT3-W (10 dB), and an HP 8470B crystal detector and a DMM-6-1500 dual balance mixer (DBM).

2. Phase-Locked Loop (PLL)

The half-power bandwidth at the resonant point of the superconducting cavity is only a few Hz. However, the frequency drift caused by external mechanical vibration is approximately 20~30 Hz. The frequency drift during cooling is approximately 0.1 MHz/K. To this end, the microwave measurement system requires a PLL technique to allow the frequency of the signal generator HP 8663A to track the frequency change of the cavity in order to ensure that the superconducting cavity remains in a resonant state.

Figure 6 shows the PLL measurement circuit. The microwave signal generated by the HP 8663A (10 mW) travels through the 20-W power amplifier, isolator, and variable attenuator to reach the HP 778D directional coupler. At that point, the main signal is directly fed into the main coupler of the superconducting cavity from the exit of the directional coupler. In addition, a -20 dB signal is extracted from the incident wave to be transmitted to one port (LO) of the

DBM after passing through a mechanical phase shifter. Another microwave signal is extracted from the superconducting cavity to be transmitted to the RF end of the DBM. A phase-error signal will be sent after comparing the two signals. This error signal goes through a PI amplifier and is then transmitted to the FM port of the HP 8663A to form a stable feedback-control circuit.

3. Main Coupler and Pick-Up Probe

The microwave power is fed into the superconducting cavity through the main coupler. The pick-up probe extracts the microwave signal from the cavity for measurement. As far as power input and pick-up signal are concerned, the external quality factors, Q_{ext}, are defined as follows:

$$Q_{ext_1} = 2\pi U/W_g \quad (\textit{input portion}), \qquad Q_{ext_2} = 2\pi U/W_p \quad (\textit{pick-up portion}) \tag{1}$$

where U is the energy stored in the cavity, and W_g and W_p represent the energy loss per cycle at the internal resistance of the signal generator and that in the signal pick-up circuit, respectively. It is known[1] that the quality factor with load, Q_1, is related to [the unloaded quality factor] Q_0 as follows:

$$1/Q_1 = 1/Q_0 + 1/Q_{ext_1} + 1/Q_{ext_2} \tag{2}$$

In order to express the degree of coupling, let us introduce the coupling factors for the input circuit and pick-up circuit as β_1 and β_2.

$$\beta_1 = Q_0/Q_{ext_1}, \qquad \beta_2 = Q_0/Q_{ext_2} \tag{3}$$

Substituting β_1 and β_2 into equation (2), we have:

$$Q_0 = Q_1\ (1 + \beta_1 + \beta_2) \tag{4}$$

The quality factor of the cavity with load, Q_1, can be measured experimentally. The unloaded quality factor, Q_0, can only be determined after β_1 and β_2 are obtained. Figure 7 is a schematic diagram of the main coupler. The Q_0 value is approximately 10^8~10^9. In order to feed as much microwave power as possible into the cavity, it is required that Q_{ext_1} of the main coupler be comparable to Q_0. Since Q_{ext_2} of the pick-up probe is two orders of magnitude higher than Q_0, the magnitude of the signal picked up by the probe has little effect on the measurement of Q_0. β_2 of the probe can be neglected in calculating Q_0.

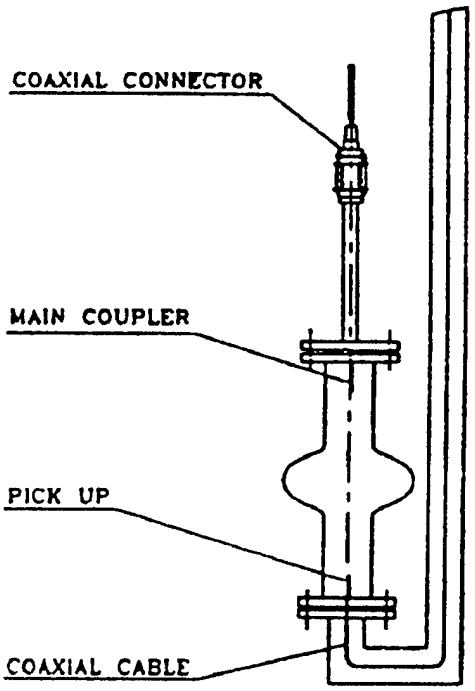

Figure 7. Main Coupler and Pick-up

The external Q values are designed to be: Q_{ext_1} = (1~3) x 10^9, Q_{ext_2} = 1 x 10^{11} and the length of the main coupler antenna and that of the probe are determined accordingly. These values were first estimated using a computer and then adjusted experimentally; finally, they were verified during superconductivity. If necessary, the devices will be reinstalled; this is a delicate piece of experimental work. At liquid-He temperature, the value of Q varies due to thermal expansion and contraction. The pick-up probe is made of a 50-Ω hard coaxial cable. During cooling, the insulating layer between the inner and outer conductor contracts several dozen times more than the metal. The result is that its Q_{ext_2} is two orders of magnitude higher than the designed value at liquid-He temperature. We encountered similar problems with the main coupler.

The antenna of the main coupler is a piece of 50-Ω coaxial cable. There is a vacuum between the inner and outer conductor. One end is connected to the power feed line through a 50-Ω coaxial ceramic seal. This ceramic connector can only operate down to 20 K. The inner conductor is made of molybdenum. The antenna and the inner conductor are threaded together. Initially, the antenna was made of copper. After the experiment, it was found that the antenna almost came loose and there was only one thread left connected. This is because copper has a higher thermal expansion coefficient than molybdenum. Through experimentation, the design was modified and materials were changed, in order to make experimental values obtained at room temperature consistent with those obtained at low temperature.

The electric field distribution, E_z, in the cavity was calculated using URMELT. Based on the relationship between probe voltage, electric field in the cavity and probe length, it is possible to estimate the length of the probe. Figure 8 shows the experimental method to measure the lengths of the antenna and the probe. An auxiliary antenna is set at one end of the cavity and its length is adjusted based on the reflective scan signal to make β = 1. The output power of the signal generator is measured with a power meter. Then, the pick-up power of the main antenna at the other end of the cavity is measured. The length of the antenna is adjusted to obtain a suitable power pick-up to output ratio. Thus, the desired external Q values can be obtained. In our experiments, Q_{ext_1} = 1 x 10^9, Q_{ext_2} = 2 x 10^{10}. The latter is one order of magnitude lower than the designed value because the phase comparator requires the probe to provide a signal higher than 5 dBm.

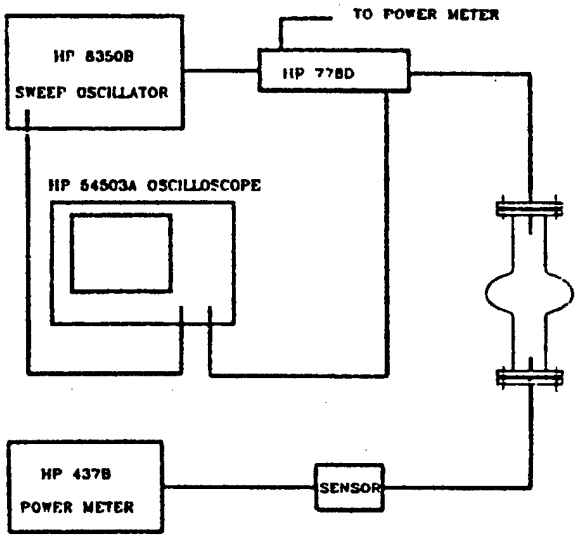

Figure 8. Principle of Q_{ext} Measurement

VI. RF Superconducting Experiments and Results

RF superconducting experiments began in October 1990. The first experiment was to test the entire low-temperature system. The low-temperature and vacuum system was found to perform well; it was safe and reliable to operate. The system is capable of pumping the Nb cavity and the cryostat jacket to 10^{-6}Pa and 10^{-4}Pa, respectively, prior to cooling. After two days at liquid-N_2 temperature, the temperature of the Nb chamber reaches 160 K. During a superconducting experiment, liquid He is transported from the Dewar to the cryostat in a pipe until the entire Nb cavity is submerged. At the same time, the recovery pipe is turned on to receive He in the low-temperature workshop. Afterward, the liquid-He pipe is removed. The temperature of the Nb cavity is 4.2 K. The level of liquid He is above the upper flange of the beam pipe. The temperature and liquid-He level are monitored with an Fe-Rh thermistor and a liquid-He-level meter, respectively. A 15-liter mechanical pump is attached to the cryostat with a three-way connector. Its exhaust is connected to the return. The reduced-pressure, low-temperature experiment can proceed by turning on the mechanical pump and controlling the valve. The lowest temperature achievable is 2 K.

1. RF Superconducting Results

The RF superconducting experiment is designed to investigate the RF characteristics of the 1.5 GHz Nb cavity in the superconducting state. This kind of L-band resonant cavity is used in a linear accelerator. Experimentally, the unloaded Q value was measured as a function of acceleration gradient, E_{acc}, and temperature, T. Temperature was varied by cooling under reduced pressure. Q values of the cavity at 6.5 K, at 4.2 K, and at several points between 4.2 K and 2 K were measured. Such measurements were made over and over again with excellent reproducibility. Figure 9 shows a curve plotting surface resistance R_s against T_c/T. The relationship between R_s and Q_0 is $G = R_s \times Q_0$, where G is the geometric constant of the cavity. For this cavity, $G = 260\ \Omega$. T_c is the critical temperature and is 9.2 K for Nb. The solid line in Figure 9 is the expected R_s versus temperature curve derived from BCS theory. The triangles are experimental points. The theoretical values are in very good agreement with experimental points in most areas. At very low temperatures, the experimental points deviate from the theoretic curve and gradually approach a fixed value. This is normal and the value is known as the residual resistance, R_{res}, of the superconducting cavity. This is also the difference between RF superconductivity and dc superconductivity. The magnitude of R_{res} is dependent on Nb surface characteristics.[1]

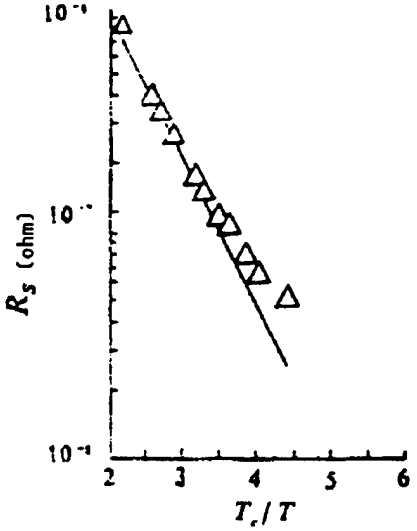

Figure 9. Curve of R_s Vs. T_c/T

Figure 10 shows the Q_0 versus E_{acc} curve. A power experiment was performed at 4.2 K and 2.25 K. Q_0 and E_{acc} were measured at various input power. As shown in

the figure, Q_0 decreases with increasing E_{acc}. The rate of decline and the presence of an obvious turning point are criteria to judge the RF characteristics of a cavity. The Q_0 versus E_{acc} curve should be relatively flat for a good cavity. At a higher gradient of acceleration, Q_0 should drop or show an apparent turning point. No turning point was found in our experiment. However, Q_0 did fall somewhat. In our initial power experiment, a gradient of acceleration of 3 MV/m was obtained. After repeatedly improving techniques such as chemical polishing, thermal treatment, reduced pressure cooling, and microwave PLL, it has been increased to 8.6 MV/m. This value is already at a world-class level. Currently, we are preparing to conduct the more difficult He experiment to further improve the Q_0 versus E_{acc} curve to obtain a larger Q_0 at higher E_{acc}.

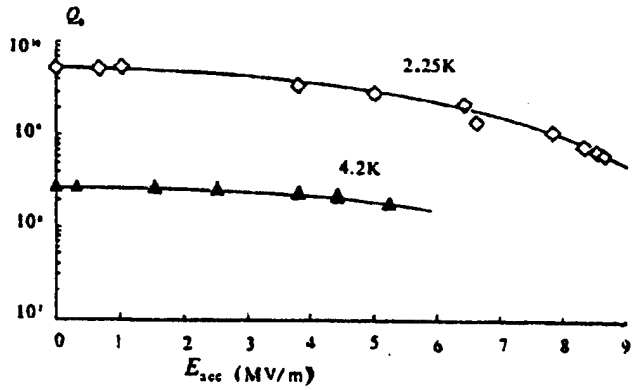

Figure 10. Q_0 Vs. E_{acc}

In the figure, E_{acc} is calculated from the following:

$$E_{acc} = (\sqrt{2}/0.1)\sqrt{102 \times Q_0 \times (4\beta/(1+\beta)^2) \times P_i} \qquad (5)$$

where 0.1 is the effective acceleration length of the cavity (m), (102 x Q_0) is the impedance of the cavity (Ω), P_i is the incident RF power (W) and E_{acc} is in units of (V/m). Values of β and Q_0 are discussed in detail in the following section.

2. Microwave Measurement Technique Under Superconducting Conditions

As mentioned earlier, the unloaded quality factor, Q_0, of the 1.5 GHz Nb cavity is 10^8~10^9 and the half-power bandwidth is only a few Hz. The field-decay time constant, however, is often as long as 30~300 ms. This makes the measurement of RF parameters and location of the resonant point very difficult. Furthermore, because our experimental cavity does not have a frequency tuning mechanism, it makes it more difficult to determine the resonant frequency.

(1) Locating the Resonant Point by Frequency Scanning

Because the HP 8663A synthesized signal generator has a very high frequency stability and a 0.4 Hz frequency scan resolution, precision scanning is carried out in every 100 Hz region between 1.46 GHz and 1.47 GHz at a rate of 100 ms/Hz. After repeated precision frequency scanning, the superconducting resonant frequency was captured. After this frequency is obtained, the generator is switched from scanning to CW mode. In addition, the PLL begins to operate. Under the control of the PLL, the superconducting cavity operates steadily in a resonant state.

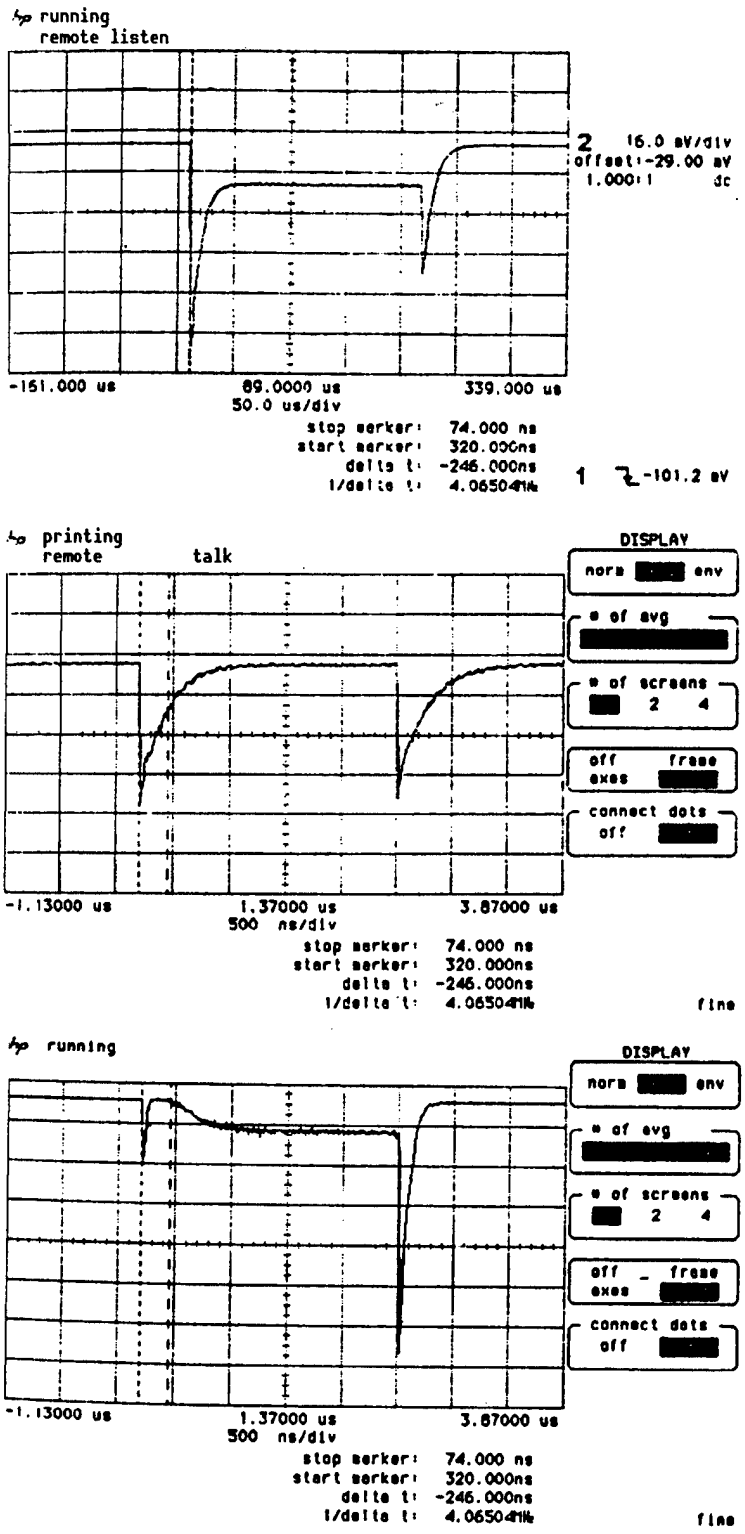

$\beta < 1$

$\beta = 1$

$\beta > 1$

Figure 11. β and Reflected Pulse

(2) Measurement of β by Reflection

The value of β is measured by using the transient response of the resonance circuit. When a pulse-modulated RF signal is fed into the cavity, the electric field inside the cavity undergoes a build-up and a decay process. By subtracting the transient incident voltage pulse from the transient cavity voltage signal, we have the transient reflected voltage signal. The shape of the reflected voltage pulse varies with β. Figure 11 shows three different reflected pulses corresponding to $\beta < 1$, $\beta = 1$, and $\beta > 1$. From transmission line theory,[10] we have

$$\beta = X/(2 - X) \tag{6}$$

where X = b/a; b is the height of the latter peak in the reflected pulse and a is the height of the earlier peak of the reflected envelope.

The transient reflected voltage of the cavity was measured at the reflected end of the HP 778D directional coupler as shown in Figure 6. Corresponding to each incident power the reflected pulse was recorded and its β value calculated.

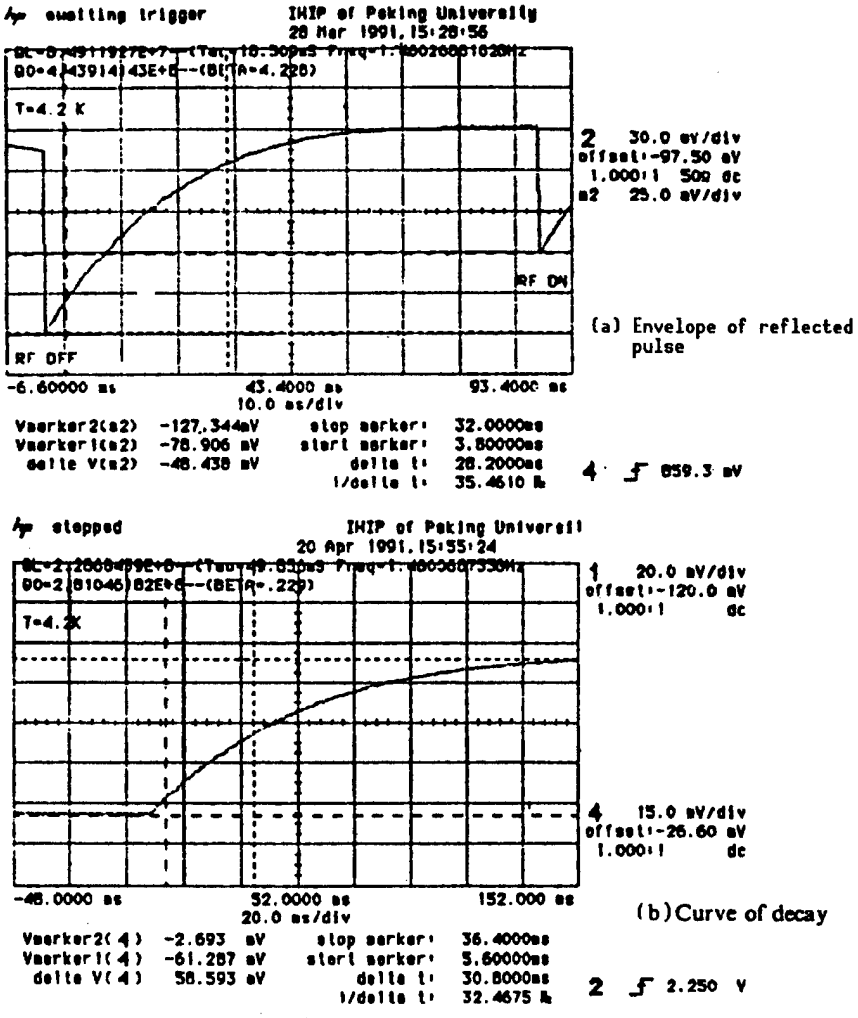

Figure 12. Measurement Results

The reflection method for measuring β is appropriate when the two peak heights are comparable. Based on an error analysis we know that the measurement error for X is seriously amplified when X approaches 2. Therefore, the external Q values of the main coupler ought to be adjusted to make its coupling factor β as close to 1 as possible to minimize any measurement error. The best way is to use a main coupler with an adjustable antenna. Figure 12 shows the reflected pulse during a superconducting cavity experiment.

(3) Measurement of Q by Decay

Experimentally, the loaded quality factor Q_1 can be measured. With the corresponding β, Q_0 can be calculated. Q_1 may be measured by frequency scanning or decay. When Q is as high as 10^8~10^9, f_0 can no longer be accurately measured by scanning. However, the decay technique is suitable for measuring a high Q value. When a stable electromagnetic field is established in the cavity, the RF signal is cut off to measure the decay curve of the field. A time constant τ can be determined from the decay curve. The value of Q_1 can be calculated from the following:

$$Q_1 = \pi \times f_0 \times \tau \tag{7}$$

where f_0 is the resonant frequency.

The other curve in Figure 12 is the free decay signal of the electromagnetic field in the cavity.

3. Control of Experimental Apparatus and Data Acquisition

In terms of microwave measurement technology, we have successfully located the resonant frequency of the high-Q cavity and kept the superconducting cavity operating in resonance with stability using a PLL technique. These methods are new to the microwave measurement field in China. In the meantime, microcomputer control and automatic data processing were made possible for the system shown in Figure 6. Programs were written for an HP PC-312 microcomputer to control the entire measurement system (signal source, oscilloscope, frequency counter, and power meter) to make measurement accurate, intuitive, fast, and convenient.

The HP PC-312 has an HP BASIC controller which has its own CPU on board. The controller board has a 2.5 MB BASIC dedicated memory for remote control and data acquisition through an HP-IB interface. The program written is specifically for the Q values of the RF system and its capabilities include on-line calculation, screen (result) printing, data storage, data display, and post data processing. A menu is used to select and modify parameters. It is simple to operate. The software is comprised of top-down modules. It has a solid structure and has a great deal of fault-tolerance. Its user interface is also friendly. The program can perform the following:

(1) Measure Q by way of frequency scanning or decay and display results on the oscilloscope screen.

(2) Print any position of the oscilloscope screen with a laser printer in four different sizes. Several figures may be printed on the same page.

(3) Oscilloscope waveform data is stored on disk for future recall, recalculation, and post treatment.

(4) Redisplay and computation of stored waveform.

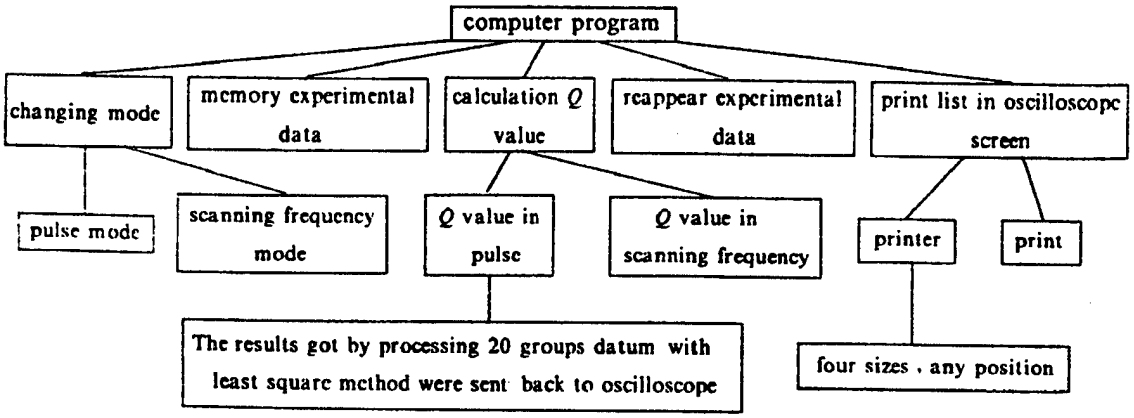

Figure 13. The Function of Program Control

Figure 13 shows a brief outline of the function of the control program. Figure 14 shows the main menu of the program. Figure 15 is a picture of the 1.5 GHz Nb superconducting cavity. Figure 16 shows the assembled Nb cavity. Figures 17 and 18 are photographs of the microwave PLL measurement system and the cryostat, respectively.

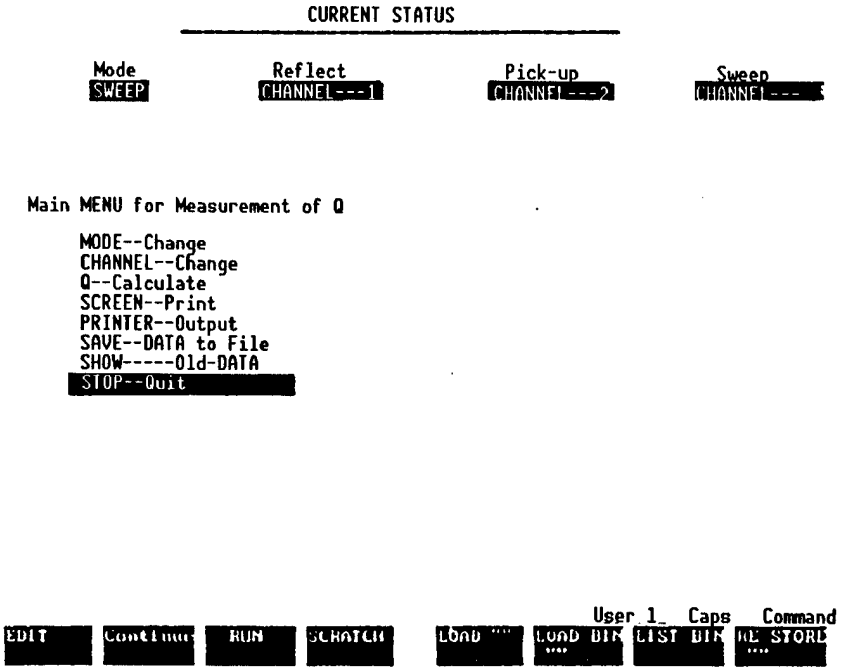

Figure 14. Main Menu of Program

The upper part of Figure 12 shows the calculated Q and β. Q_0 can be derived based on these numbers. Program controlled automatic measurement is very convenient and timely. It improved our efficiency and success rate.

VII. Conclusions

The superconducting cavity group at the Institute of Heavy Ion Physics of Beijing University has made significant progress in the study of the RF superconducting cavity in a relatively short period of time. This research will serve as a basis and technical foundation for future use of the RF superconducting cavity and development of superconducting high-brightness electron injectors.

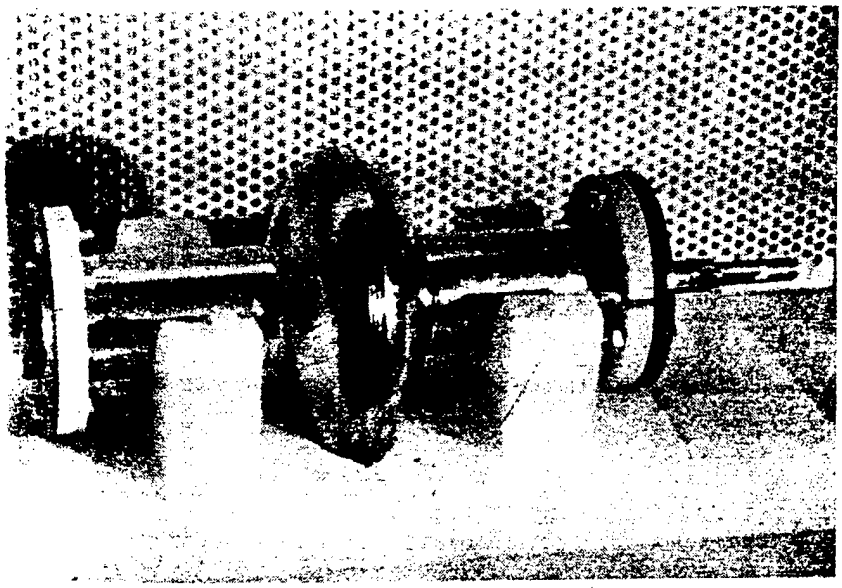

Figure 15. 1.5 GHz Nb Superconducting Cavity

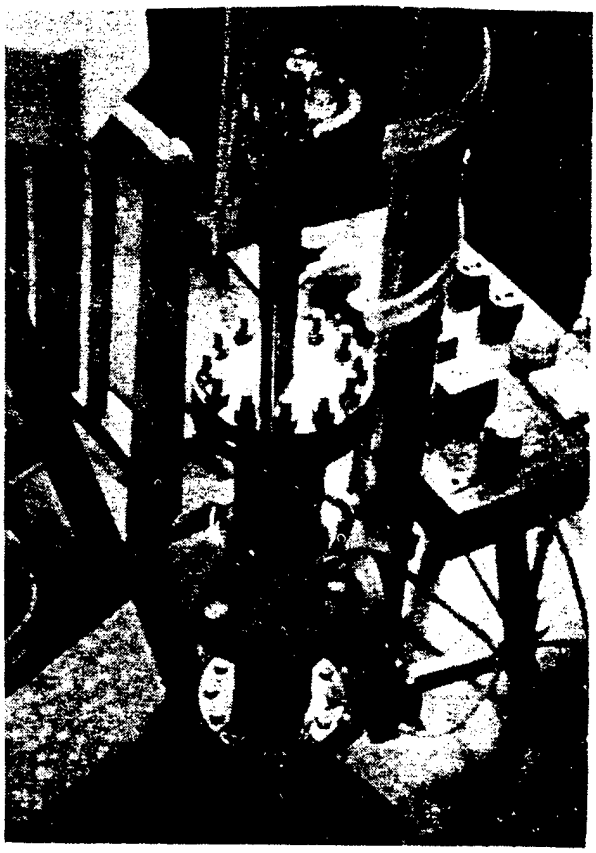

Figure 16. Fixed Nb Cavity

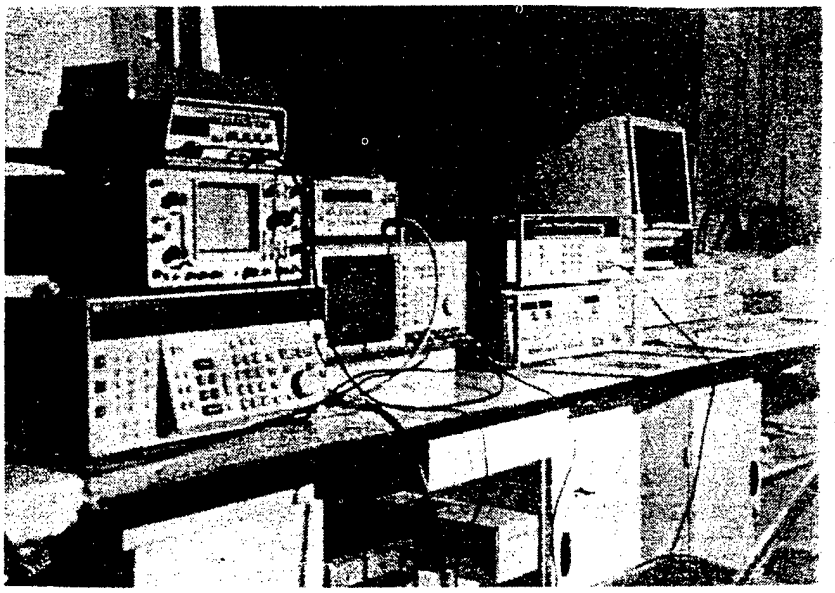

Figure 17. Microwave Measurement System

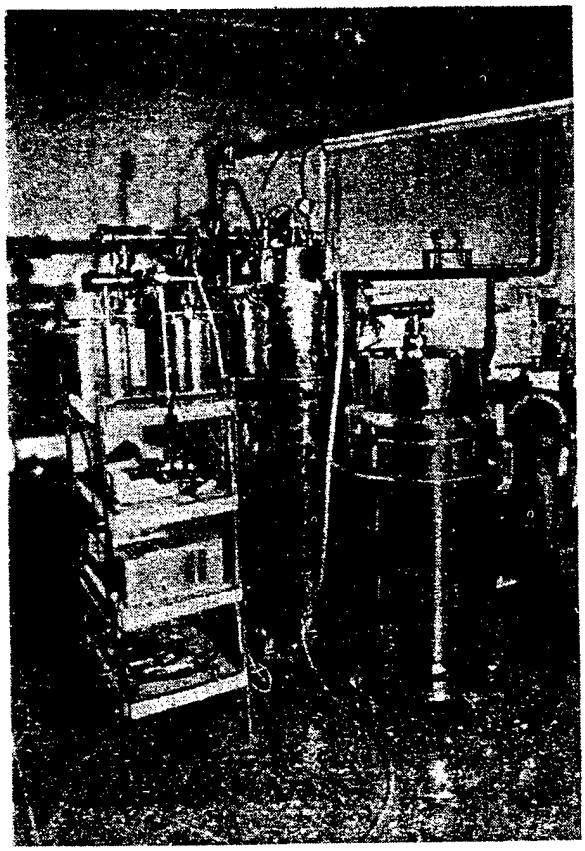

Figure 18. Photo of Cryostat

Acknowledgement

First, the authors wish to thank the concerns and support of some experts and the leadership at Beijing University. In the past three years, Shen Zilin [3088 1311 2651], Lu Dequan [0712 1795 3123], Wu Huimin [6762 1920 3046], Fu Xiaobin [0102 0879 2430], and Geng Rongli [5105 2837 4409] of the Institute of Heavy Ion Physics participated in the superconducting cavity work. Teachers and engineers at the Low-Temperature Workshop of the Physics Department at Beijing University worked hard to support the supply of liquid N_2 and He and to ensure the recovery of He. Professors Liu Weilang [0491 1792 3186] and Dai Yuandong [2071 6678 2639] personally guided the transport of liquid He for cooling to ensure the safety of the experiment.

The authors also wish to thank Dr. D. Proch of DESY, Dr. H. Padamsee of Cornell University, Dr. T. Weiland of Darmstadt, and Professor Tong Dechun [4547 1779 2504] of Qinghua University for their support and assistance.

References

1. H. Piel, CERN 89-94, 1989, p 149.

2. Wang Guangwei, et al., "Study of RF Superconducting Cavity and Its Characteristics," Beijing University Institute of Heavy Ion Physics Report SC-91-03, 1991.

3. L. Serafini, et al., EPAC 90, 1990, p 143.

4. D.L. Moffat, et al., KEK Report 89-21, 1990, p 445.

5. D. Proch, et al., DESY M-84-10, 1984.

6. K. Saito, et al., KEK Report 89-21, 1990, p 635.

7. D. Bloess, et al., KEK Report 89-21, 1990, p 477.

8. H. Lengeler, CERN 89-04, 1989, p 197.

9. K.C.D. Chen, Proceedings of the Beijing FEL Seminar, 1988, p 172.

10. Song Jinhu, "Experimental Study on Superconducting Resonant Cavity," Master's Thesis of the Department of Technical Physics, Beijing University, 1991.

11. Zhao Kui, et al., "Large-Gradient Superconducting Resonant Cavity," Proceedings of the Accelerator Conference, 1988.

12. Chen Jiaer, et al., "RF Superconducting Cavities at IHIP of Beijing University," to be published, 1990.

13. Chen Jiaer, et al., IHIP Report SC-91-01, 1991.

14. Q.S. Shu, KEK Report 89-21, 1990, p 539.

15. R.W. Roth, et al., EPAC 90, Nice, 1990.

16. B. Byrns, et al., EPAC 90, Nice, 1990.

17. K. Asano, et al., KEK Report 89-21, 1990, p 723.

18. G. Mueller, KEK Report 89-21,1990, p 267.

19. K.W. Shepard, KEK Report 89-21, 1990, p 139.

Design of Time-Dependent E-Beam Spectra Diagnostics for Beijing FEL

92FE0442B Chengdu QIANG JIGUANG YU LIZI SHU [HIGH POWER LASER AND PARTICLE BEAMS] in Chinese Vol 4 No 1, Feb 92 pp 33-40

[Article by Zhao Xiaofeng [6392 1420 7364], Yi Kaiqi [4135 7030 4388], Zhang Jian [1728 0494], Wei Qiong [7614 8825], Sheng Shugang [4141 2885 0474], Zhou Qiaogen [0719 1564 2704], and Zhang Huimin [1728 1920 3046] of Shanghai Institute for Nuclear Research, 201800, and Li Yunshan [2621 0061 1472], Zhuang Jiejia [8369 2638 0163], Chen Yuanbai [7115 0337 2672], Zheng Shuchen [6774 2885 5256], Ou Yang [2962 7122], Li Zhigang [2621 1807 0474], and Mao Chengshen [3029 2052 3932] of the Beijing Institute of High-Energy Physics, P.O. Box 918, Beijing 100039: "Design of Time-Dependent E-Beam Spectra Diagnostics for Beijing FEL"; MS received 8 Nov 90, revised 4 Jul 91]

[Text] **Abstract**

The electron beam (e-beam) from the wiggler, after passing through the 180° bend, enters the energy and time spectrum diagnostic system. The 180° bend is designed for achromatic and isochronous transport of the e-beam. Isochronous transport satisfies the diagnosis of the time resolution of micropulses and achromatic transport satisfies the diagnosis of the time resolution of macropulses. The time-dependent macropulse energy spectrometer is comprised of four matching lenses, a two-slit device, a sweep deflector coil, a 90° symmetric bifocal analyzing magnet, a fluorescent target at the focal plane, a video camera system with an image intensifier, and an on-line computer-based graphics processing system. Its energy resolution is better than 1,000 and time resolution is higher than 60 ns.

[Introduction]

Figure 1 shows the layout of the diagnostics for the time-dependent energy spectra of micro and macropulses of the e-beam of the Beijing FEL. Limited by available space, the e-beam from the wiggler must be bent by 180° before entering the time-dependent energy spectrometer system. This paper describes the 180° bend and the macropulse diagnostic system.

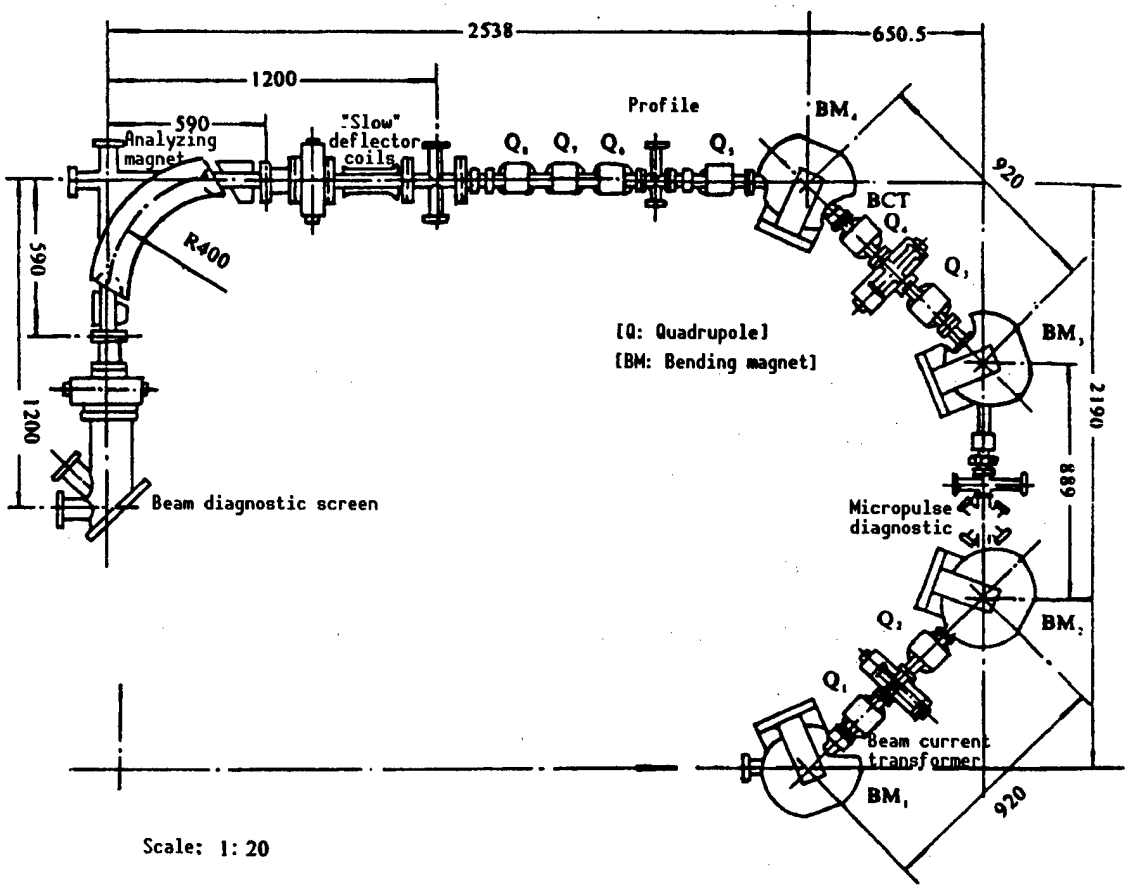

Figure 1. Beamline Configuration for E-Beam Diagnostics of Beijing FEL

I. Design of the Isochronous and Achromatic Bend

The 180° bend may be designed for either isochronous or achromatic transport, or both. Isochronous transport satisfies the diagnostics of the micropulse time spectrum I(t) and achromatic transport satisfies the diagnostics of the time-dependent macropulse energy spectrum I(E,t).

For a system comprised of a horizontal bending magnet, a quadrupole lens and a drift segment, its first-order six-dimensional transport matrix is as follows[1]:

$$\begin{bmatrix} M_{11} & M_{12} & 0 & 0 & 0 & M_{16} \\ M_{21} & M_{22} & 0 & 0 & 0 & M_{26} \\ 0 & 0 & M_{33} & M_{34} & 0 & 0 \\ 0 & 0 & M_{43} & M_{44} & 0 & 0 \\ M_{51} & M_{52} & 0 & 0 & 1 & M_{56} \\ 0 & 0 & 0 & 0 & 0 & 1 \end{bmatrix} \quad (1)$$

Furthermore, when it satisfies the following conditions:

$$\begin{cases} M_{16} = 0 \\ M_{26} = 0 \end{cases} \tag{2}$$

it is achromatic. This means that the emissivity of the e-beam does not increase as it passes through the system despite the fact that its energy is dispersed. When

$$\begin{cases} M_{51} = 0 \\ M_{52} = 0 \\ M_{56} = 0 \end{cases} \tag{3}$$

the system is an isochronous transport system. This means that the deviations in trajectory and energy of the e-beam are independent of the initial motion on the bending plane and the longitudinal length of the electron cluster remains unchanged.

In engineering terms, equations (2) and (3) imply that the system must have at least five optical elements, such as quadrupole lenses, to provide complicated adjustments and diagnostics to put the system in isochronous and achromatic operation. Obviously, this is very inconvenient. To simplify the design and for ease of use, the 180° bend was designed symmetrically. Equations (2) and (3) can be simplified and the transport matrix elements at the center of the system (on the symmetry plane) can be made to satisfy the following conditions (proof for isochronous and achromatic transport is omitted).

$$\overline{M}_{26} = 0 \tag{4}$$

$$\begin{cases} \overline{M}_{22}\overline{M}_{51} - \overline{M}_{21}\overline{M}_{52} = 0 \\ \overline{M}_{56} + \overline{M}_{26}(\overline{M}_{51}\overline{M}_{21} - \overline{M}_{52}\overline{M}_{11}) = 0 \end{cases} \tag{5}$$

In practice, two optical elements for adjusting the beam parameters can be eliminated. Considering the fact that the streak camera used to measure the Cerenkov radiation of the micropulse is a block-type measurement, i.e., micropulse and macropulse diagnostics cannot be done simultaneously, the 180° bend was designed to have two pairs of symmetric quadrapole lenses (each pair in series). When performing macropulse diagnostics, only one pair is required.

This kind of symmetric bend has several advantages. For example, when the system operates in the achromatic mode, equation (4) becomes:

$$\begin{aligned} &[\overline{H}_{22}Q_{21} + \overline{H}_{21}(Q_{11} + l_2Q_{21})](H_{16} + H_{26}l_1) \\ &\quad + [(Q_{12} + l_2Q_{22})\overline{H}_{21} + Q_{22}\overline{H}_{22}]H_{26} + \overline{H}_{26} = 0 \end{aligned} \tag{6}$$

where H, $\overline{H}$, and Q are the transport matrixes of the first bending magnet, second bending magnet, and quadrapole lens, respectively; l_1 and l_2 are the distance from the exit of the first bending magnet to the inlet of the lens and the distance from the exit of the lens to the inlet of the second bending

magnet, respectively. By substituting the parameters of or system into equation (6), we have

$$24.787\ k\sin kl - 0.03965\ \frac{\sinh k\,l}{k} - 2.6895\cos kl - 0.707 = 0$$

where $k = (G/p)^{1/2}$, G is the gradient of the lens (Gs/cm), p is the electron magnetic rigidity (Gs-cm), and l is the effective length of the lens (l = 10 cm). A unique solution of k may be obtained from this transcendental equation. In practice, the excitation current of the lens, I_Q, is set based on the magnitude of the excitation current of the bending magnet (i.e., electron magnetic rigidity), I_B, to make $k = k_0$ which puts the system in the achromatic mode. Furthermore, the I_Q~I_B curve also serves as an operational curve which is precalculated. When the system is set for the isochronous mode, there is another set of I_{Q1}, I_{Q2}~I_B curves. Similarly, these curves can be calculated in advance.

In mid-1990, the Beijing FEL group requested that the micropulse measurement system be installed behind the first 90° bend. The original achromatic design for macropulse diagnostics was not affected by this decision. However, the symmetric isochronous transport design would not meet the requirements for micropulse diagnostics. In operation, careful adjustments of the parameters of the two lenses in the first 90° bend are required to achieve isochronous transport in the 90° bend. Computation done with the TRANSPORT program[1] indicates that isochronous transport is still possible in this case to meet the requirement for micropulse diagnostics. Furthermore, the calculated results can provide guidance for operation. Figure 2 shows the calculated e-beam envelope in achromatic and isochronous transport. The initial state of the e-beam is that it is in the center of the wiggler. The e-beam has two waists and the diameter of the waist is 1 mm. The normalized emissivity is 30π mm-mrad. The focusing in the y direction provided by the B_z component of the wiggler field is linearized as follows:

$$\begin{bmatrix} y \\ y' \end{bmatrix} = \begin{bmatrix} \cos(z/\beta_c) & \beta_c \sin(z/\beta_c) \\ (-1/\beta_c)\sin(z/\beta_c) & \cos(z/\beta_c) \end{bmatrix} \begin{bmatrix} y \\ y' \end{bmatrix}_{z=0} \tag{7}$$

where $$\beta_c = N\ \lambda_w/2\pi.$$

N is the number of periods of the wiggler field and λ_w = 3 cm.

II. Macropulse Time-Dependent Energy Spectrometer

The system consists of four matching quadrupoles (after a 180° bend), a double slit device, a deflector sweep coil, a 90° symmetric bifocal analyzing magnet, a fluorescent target at the focal plane, a video camera with image intensifier, and an on-line computer graphics system (Figure 1). The following is a description of the design of major components.

1. 90° Bifocal Analyzing Magnet

After achromatic bending of 180°, the e-beam is transformed into a double waist (object) at the horizontal slit of the double-slit device. An image is formed on the fluorescent target after passing through the 90° bifocal analyzing magnet. This analyzing magnet is designed to be symmetrically bifocal for more stable operation. Its bending radius R = 400 mm, horizontal dispersion D_H = 4, and amplification factor M = 1. With a full object slit width of 1.6 mm, the energy resolution is 1,000. This means that 10 measurement points can be obtained on the focal plane for an e-beam with a ±0.5% energy dispersion. In this case, the full image width is 16 mm. The designed maximum e-beam energy dispersion is ±3%, which corresponds to a full image width of 96 mm.

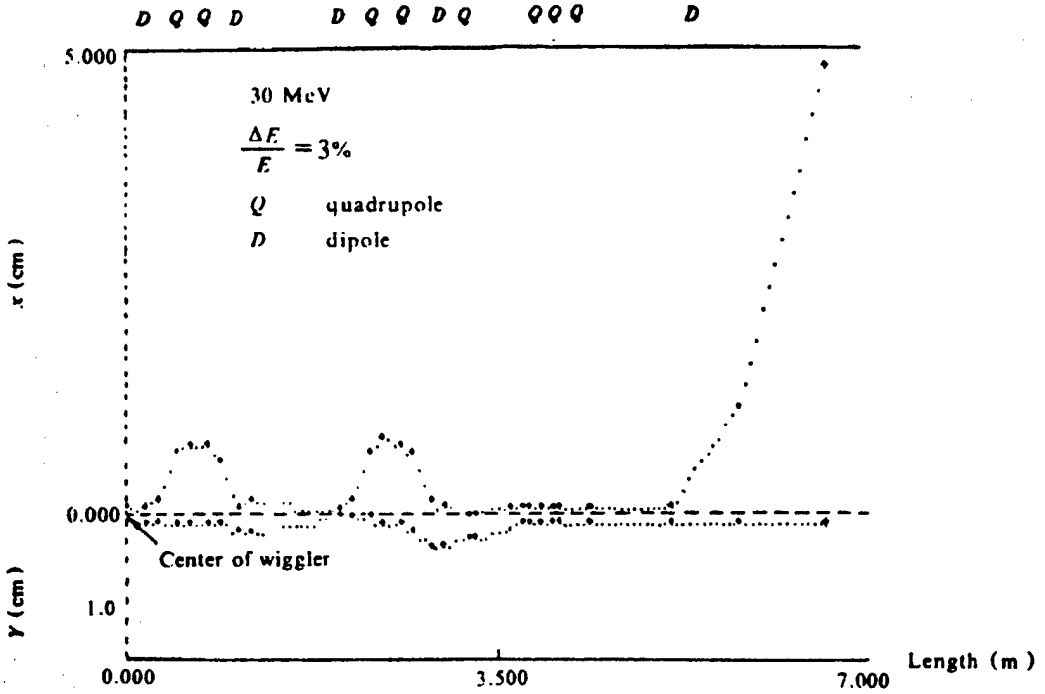

Figure 2. Envelope of Electron Beam

In order to ensure magnetic field uniformity in the working area (better than 10^{-3}), the width of the pole is four times the air gap between poles. The operating magnetic flux is 0.1~0.35 T. In order to ensure the same effective hard magnetic boundary at different field strengths, the boundary is designed to be a Rogowski approximation boundary with magnetic shield clamping. The incident and emergent angles of the analyzing magnet are designed to be tunable over the range of 25° ± 15° so that the actual incident and emergent angles may be adjusted according to the measured edge field distribution. Furthermore, this arrangement will make it more convenient in the future to compensate for aberrations near the poles with a circular arc boundary provided by a hexapole field. Figure 3 shows the uniform field distribution calculated using the POISSON program.[2] The data (Table 1) indicates that the uniform region is over 4 cm wide.

Computation done with the TRANSPORT program shows that when the normalized emissivity of the e-beam is 30π mm-mrad, the object slit can vary between 1.2 and 1.6 mm without affecting the transport characteristics of the system. The corresponding resolution of the energy spectrometer is 1,300~1,000.

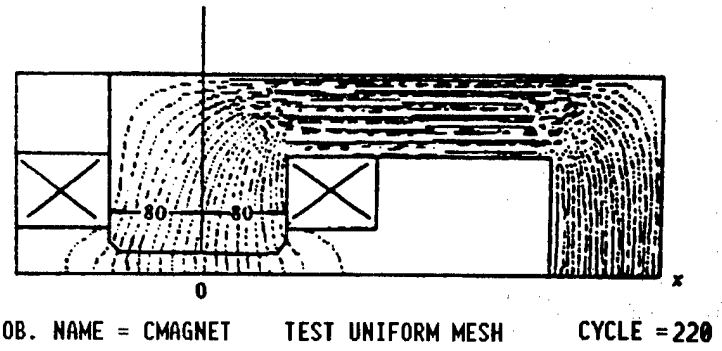

Figure 3. Calculated Results of the POISSON Program

Table 1.

x (mm)	-30	-15	+15	+30
$\Delta B/B_0$	5.4×10^{-4}	1.6×10^{-4}	5.7×10^{-5}	5.8×10^{-4}

2. Sweep Deflector Coil

The diagnostics of the time-dependent macropulse energy spectrum I(E,t) are accomplished by a vertically sweeping e-beam generated by a sweep deflector coil within a macropulse. In this case, the vertical beam size on the planar fluorescent target represents the width of the macropulse. The macropulse width of the Beijing FEL is 2~5 μs. Hence, the sweeping magnetic field rises very rapidly. In order to avoid a very large inverse peak voltage between the magnetic pulsed power supply and the excitation coil, a low-inductance coreless saddle-shaped deflector coil is used to generate the uniform bipolar magnetic field. The coil, whose structure is shown in Figure 4, is split into two symmetric halves which are tightly wrapped around the beam pipe. The angular distribution of the number of windings varies in a manner close to a cosine function. Since the coil inductance increases with the square of the number of windings, the number of windings should be as small as possible. However, the fewer the number of windings, the poorer the uniformity of the bipolar field and the larger the error of the diagnostics of the time-dependent

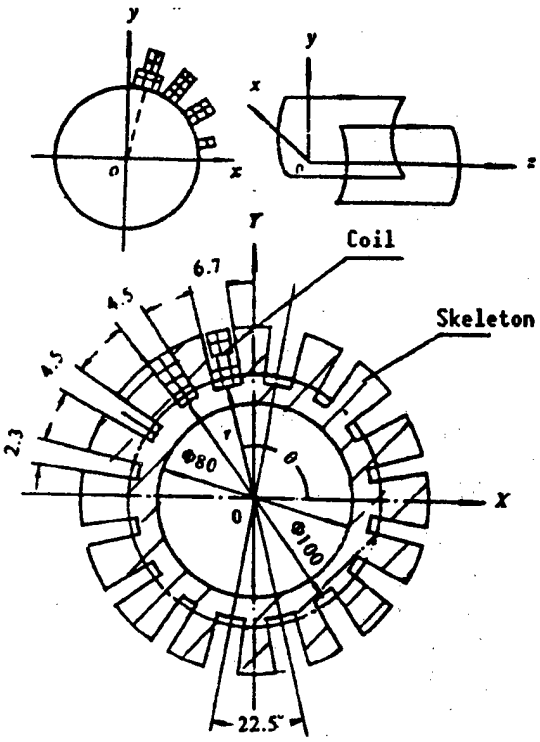

Figure 4. Scheme of Slow-Deflector Sweep Coil

spectrum. We were required to use the smallest number of windings provided that the uniformity of the field is less than 1 percent. A variety of schemes were compared by computation using the MPVP program[3] and by actual measurements using a simulator. The final design chosen has a total of 52 windings and its angular distribution is shown in Figure 4. The conductor is a flat copper wire doubly wrapped with glass and has a cross section of 1.8 x 2.65 mm. According to actual measurements,[4] the uniformity of the bipolar field is better than 1 percent when R ≤ 15 mm. The total inductance of the deflector coil is 257 μH.

If the uniform bipolar magnetic field B generated by the deflector coil rises linearly with time, then the following relation exists when the e-beam is deflected by a small angle δ (Figure 5):

$$B = \frac{200\sqrt{E^2 + 2EE_0}}{3l(L + l/2)} Y \tag{8}$$

where E is the kinetic energy of the e-beam (MeV), E_0 = 0.511 MeV, L is the distance from the exit of the deflector coil to the fluorescent target (m), Y is the vertical coordinate of the scanned e-beam on the fluorescent target (m), and l is the effective length of the deflector coil. Actual measurements showed that l = 0.2032 m and L = 1.8783 M. In order to have the image of a 35 MeV e-beam fall at Y = 25 mm, the deflecting magnetic field should be:

$$B = \frac{200\sqrt{35^2 + 2 \times 0.511 \times 35}}{3 \times 0.2032(1.8783 + 0.1016)} \times 0.025 = 146.3\,(Gs)$$

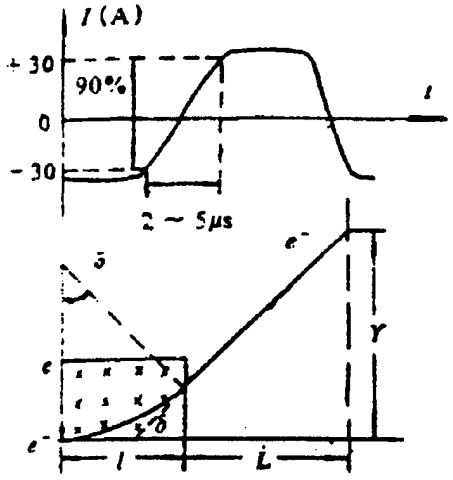

Figure 5. Relation Between Drive Current and Deflecting Power of the Sweep Coil

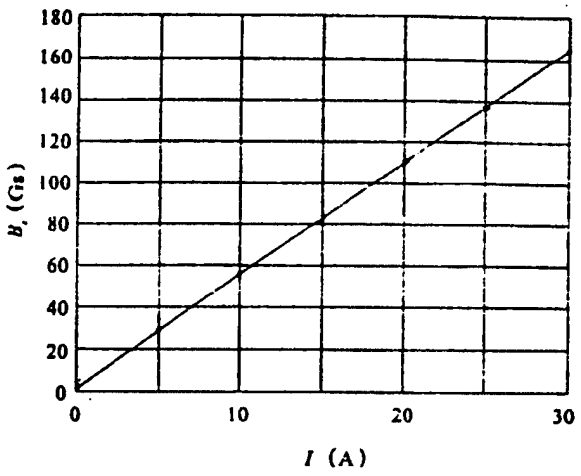

Figure 6. Magnet Excitation Curve of the Sweep Coil

Figure 6 is the measured magnetic excitation curve of the deflector coil. It is obvious that the excitation current required is less than 30 A. The design specification of the magnetic excitation pulsed power supply is that the pulse

current amplitude is ±30 A. The leading edge rises linearly and the rise time is 2~5 μs, adjustable at different scales. This power supply is being developed. The maximum inverse peak voltage of the deflector coil is:

$$L\frac{dI}{dt} = 257 \times 10^{-6} \times \frac{60}{2 \times 10^{-6}} = 7.71 \ (kV)$$

which meets the voltage breakdown requirement of the amplifier of the power supply.

Because the vertical "object slit" is designed to be 1/6 mm in full width, the effective working width of the fluorescent target in the vertical direction is 50 mm. Hence, within a macropulse, it is possible to obtain 30 points in the time-dependent energy spectrum for diagnostics. For a macropulse which is 2~5 μs wide, the camera is required to have a resolution of better than 60~150 ns.

3. Fluorescent Target, Video Camera, and Computer Graphics Processing System

An imported French-made Cr-activated Al_2O_3 fluorescent target (AF995R) with an effective working area of 100 x 50 mm was used. The TV video camera used is a Model SGB-11N, which has 350 vertical lines (<0.2 mm) and 550 horizontal lines (<0.2 mm) and a time resolution of approximately 8 ns. The camera is equipped with a microchannel-plate light intensifier and the amplification factor is 10,000. Further, the applied bias voltage between microchannels can be used for high-speed shutter control. The shortest gate control interval is several dozen nanoseconds. Therefore, it can be used to take the energy spectra of the e-beam at different intervals within the same macropulse in order to study imortant mechanisms such as the buildup process of the FEL oscillation and the emission efficiency of a micropulse. Figure 7 shows a block diagram of the image processing system.

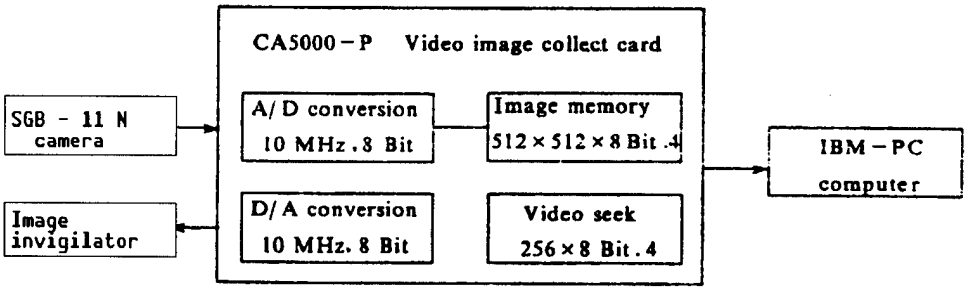

Figure 7. Block Diagram of Image Processing

The CA5000-P video image acquisition card can be directly plugged into an IBM-PC. The following figures, tables, and data can be provided on-line by the energy spectrometer by using the image processing software and FEL research software.

a. Macropulse time-dependent energy spectra (current vs. energy, current vs. time, energy dispersion vs. time, instantaneous current vs.time, etc.).

b. FEL emission efficiency.

References

1. K.L. Broun, SLAC-75 and CERN 80-04.

2. LANL Accelerator Code Group, LA-UR-87-126.

3. Zhou Qiaogen, "Method and Program for Computing the Field of an Arbitrary Current-Carrying Conductor," Proceedings of the Changsha FEL Symposium, 1990.

4. Zhang Jian, et al., "Design of a Fast-Rise Homogeneous Magnetic Dipole Coil," Proceedings of the Changsha FEL Symposium, 1990.

Analytical Research on Mode Locking in IR Short-Pulse FEL

92FE0442C Chengdu QIANG JIGUANG YU LIZI SHU [HIGH POWER LASER AND PARTICLE BEAMS] in Chinese Vol 4 No 1, Feb 92 pp 47-52

[Article by Ding Wu [0002 2976] and Du Xiangwan [2629 4382 3834] of the Beijing Institute of Applied Physics and Computational Mathematics, P.O. Box 8009, Beijing 100088: "Analytical Research on Mode Locking in IR Short-Pulse FEL"; MS received 10 May 91, revised 25 Sep 91]

[Text] **Abstract**

An analytical study is done on mode locking in an FEL (free electron laser) and the mode-locking conditions are obtained. It is derived that due to mode coupling the number of active modes in the cavity is reduced by a factor of m_c, the low gain factor is increased by a factor of m_c, and the exponential growth factor goes up by a factor of $m_c^{1/3}$; m_c is the ratio of the micropulse repetition frequency $\Delta\nu_r$ to the frequency interval of modes in the cavity $\Delta\nu_c$, i.e., $m_c = \Delta\nu_r/\Delta\nu_c$.

I. Introduction

In an RF-Linac-driven IR short-pulse FEL, when the micropulse length L_b is comparable to the total slip between the wiggler and the light beam Δ, i.e., $L_b \approx \Delta$, the propagation of the e-beam, i.e., the nonsteady-state term, must be taken into account in the equation. The mode locking under such conditions has been investigated by numerical modeling in reference [1]. However, when the length of the micropulse, L_b, is still much larger than the total slip between the wiggler and the light beam Δ, i.e., $L_b \gg \Delta$ (such as $\tau_b \sim$ 10 ps, $\lambda_s \sim 1$ μm, $L_b = \nu_z \tau_b \approx 0.3$ cm, $\Delta = N_w \lambda_s \approx 100 \times 10^{-4}$cm = 0.01 cm), the slip effect between the e-beam and the light beam can be neglected. It can be treated as a steady state. The mode-locking problem in this case can be studied analytically. This is an attempt to analytically study the mode-locking conditions and mode-coupling gain of an IR short-pulse FEL.

II. Gain of Coupled Mode IR Short-Pulse FEL

1. E-Beam Pulse Profile

Let us assume that the e-beam pulse follows a Guassian profile, i.e.,

$$n(t_0) = n_0 f(t_0) \tag{1}$$

$$f(t_0) = \frac{1}{\sqrt{2\pi}} \frac{v_z T_b}{\sigma_z} e^{-v_z^2 t_0^2 / 2\sigma_z^2} \tag{2}$$

where n_0, ν_z, σ_z and T_b are the density, longitudinal velocity, mean square root of the spatial length of the pulse, and time width of the pulse, respectively.

2. Optical Mode Evolution Equation

If the e-beam pulse length is still greater than the overall slip between the e-beam passing through the wiggler and the light beam, the problem can still be treated as a steady-state case. According to reference [2], the equation for the FEL longitudinal mode which takes the pulse structure of the e-beam into consideration is as follows:

With a linearly polarized wiggler, we have

$$\frac{\partial a_n(Z)}{\partial z} = \frac{\omega_b^2 a_w F_B}{4 c \gamma_0 \omega_n} e^{-i\Delta k_n z} \frac{1}{T_b} \int_{-\frac{T_b}{2}}^{\frac{T_b}{2}} dt_0 f(t_0) e^{i\omega_n t_0} F_n(z, t_0) \tag{3}$$

$$a_n = \frac{eE_n(z)}{\sqrt{2}mc^2 k_n} \tag{4}$$

$$a_w = \frac{eB_w}{\sqrt{2}mc^2 k_w} \tag{5}$$

$$\omega_b^2 = \frac{4\pi e^2 n_0}{m} \tag{6}$$

$$F_B = J_0(\xi) - J_1(\xi) \tag{7}$$

$$\xi = \frac{a_w^2}{2(1+a_w^2)} \tag{8}$$

$$\Delta k_n = k_w - k_n \left(\frac{1}{\beta_{//}^{(0)}} - 1 \right) \tag{9}$$

$$\frac{\omega_n}{c} = \frac{2 k_w \gamma_0^2}{\mu^2} \tag{10}$$

where E_n, ω_n, and k_n are the complex optical field, frequency, and wave number of mode n, respectively; e, m, and n_0 are the charge, mass, and beam density of the electron, respectively; B_w and k_w are the amplitude and wave number of the wiggler field; and J_0 and J_1 are the zeroth- and first-order Bessel functions of the first kind.

In an FEL, due to the structure of the e-beam, mode coupling can occur in the linear region. Hence,

$$F_n(z,t_0) = \exp\{-\frac{i\omega_n}{c}\sum_m e^{-i\omega_m t_0}\int L_m a_m\} = 1 - \frac{i\omega_n}{c}\sum_m e^{-i\omega_m t_0}\int_0^z L_m a_m dz \tag{11}$$

$$L_m = -\frac{\mu^2}{\gamma_0^3}\int_0^{z'}\frac{a_\omega}{\gamma_0}F_B(\frac{\omega_m}{\omega_n}\xi)\,k_m e^{i\Delta k_m z''}dz'' \tag{12}$$

By substituting equations (11) and (12) into (3), we have

$$\frac{\partial a_n(z)}{\partial z} = \frac{\omega_b^2 a_w F_B(\xi)}{4c\gamma_0\omega_n}e^{-i\Delta k_n z}\frac{1}{T_b}\int_{-\frac{T_b}{2}}^{\frac{T_b}{2}}dt_0 f(t_0)\,e^{i\omega_n t_0}$$

$$+ i\frac{\omega_b^2 a_w^2 F_B(\xi)\,(2k_w)^2}{4c\gamma_0\omega_n\mu^2}e^{-i\Delta k_n z}\frac{1}{T_b}\int_{-\frac{T_b}{2}}^{\frac{T_b}{2}}dt_0 f(t_0)\,x\,e^{i\omega_n t_0}\sum_m e^{-i\omega_m t_0}\frac{\omega_m}{\omega_n}F_B(\frac{\omega_m}{\omega_n}\xi)$$

$$x\int_0^z dz'\int_0^{z'}dz''e^{i\Delta k_m z''}a_m(z'') \tag{13}$$

Let

$$\tilde{f}_1 = \frac{1}{T_b}\int_{-\frac{T_b}{2}}^{\frac{T_b}{2}}dt_0 f(t_0)\,e^{i\omega_n t_0} \tag{14}$$

$$\tilde{f}_2 = \frac{1}{T_b}\int_{-\frac{T_b}{2}}^{\frac{T_b}{2}}dt_0 f(t_0)\,e^{i(\omega_n-\omega_m)t_0} \tag{15}$$

By substituting equation (2) into (14) and (15), we have

$$\tilde{f}_1 = e^{-\omega_n^2\sigma_z^2/2v_z^2} \tag{16}$$

$$\tilde{f}_2 = e^{-(\omega_n-\omega_m)^2\sigma_z^2/2v_z^2} \tag{17}$$

For an IR short-pulse FEL,

$$\frac{\omega_s}{v_z} \approx \frac{\omega_n}{c} \approx 10^4\,(1/cm)$$

$$\sigma_z = \frac{L_b}{\sqrt{2}} \approx 10^{-1}cm$$

$$\therefore\ (\frac{\omega_n\sigma_z}{v_z})^2 \approx 10^6$$

$$\therefore\ \tilde{f}_1 = 0 \tag{18}$$

By substituting equations (17) and (18) into (13), we have

$$\frac{\partial a_n(z)}{\partial z} = i\frac{\omega_b^2 a_W^2 F_B(\xi)\,(2k_w)^2 e^{-i\Delta k_n z}}{4c\gamma_0\omega_n\mu^2}\sum_m e^{-\frac{(\omega_n-\omega_m)^2\sigma_z^2}{2v_z^2}}$$

$$x\,\frac{\omega_m}{\omega_n}F_B\left(\frac{\omega_m}{\omega_n}\xi\right)\int_0^z dz'\int_0^{z'} dz'' e^{i\Delta k_n z''} a_m(z'') \qquad (19)$$

Equation (19) is the mode-evolution equation of the IR short-pulse FEL. As we can see, if the following inequality is valid:

$$\frac{(\omega_n-\omega_m)^2\sigma_z^2}{v_z^2} < 1 \qquad (20)$$

then it is possible to couple several modes. From equation (20), the pulse length of the e-beam is dependent on the number of coupled modes. This is because the farther apart ω_m from ω_n is, or the larger the number of coupled modes, then the shorter σ_z is required to be to keep equation (20) valid.

3. Number of Coupled Modes

According to reference [1], the number of modes that can be simultaneously activated in the resonant cavity is

$$m_g = \frac{\Delta\nu_g}{\Delta\nu_c} \qquad (21)$$

where $\Delta\nu_g$ is the gain bandwidth. It is at least determined by the uniform-gain bandwidth and $\Delta\nu_g \geq \nu_s/2N_w$, where ν_s is the center frequency of the light beam, N_w is the number of periods of the wiggler field, and $\Delta\nu_c$ is the frequency interval between modes in the resonant cavity; $\Delta\nu_c = c/2L_c$, where L_c is the length of the resonant cavity which is at least equal to L_w and L_w is the length of the wiggler.

$$\therefore m_g > \frac{\nu_s}{2N_w}\,\frac{2L_w}{c} = \frac{\lambda_w}{\lambda_s} > \gamma_0^2 \qquad (22)$$

Therefore, thousands of modes may be simultaneously activated in the cavity.

In reality, the number of activated modes decreases with growing coherent length. Nevertheless, this kind of growth is limited by the pulse length. The shorter the pulse length, the larger the number of activated modes.

As described in reference [1], an interferometer inside the cavity (e.g., a slightly oblique etalon) might be used to turn independent pulses into coherent light pulses. The number of light pulses that might be coupled is determined by the number of independent coherent pulses. The number of independent pulses is further determined by the repetition frequency of the e-beam pulse. Since we adjust the length of the etalon with respect to the

repetition frequency of the e-beam pulses so that the pulses in the etalon overlap with the new ones, the number of modes to be coupled can be determined by the following equation:

$$m_c = \frac{\Delta\nu_r}{\Delta\nu_c} \tag{23}$$

where $\Delta\nu_r$ is the repetition frequency of the electron micropulses. It is given in reference [1] that $L_c = 6$ m, $\Delta\nu_r = 1$ GHz and $m_c = 40$.

From the number of coherent pulses, $m_c = 40$, the maximum difference between the frequency of the coupled mode and the given laser frequency ω_n can be calculated. By substituting this difference and the given electron pulse length of $\sigma_z \approx 0.1$ cm into equation (20), it is found that the equation is valid. Hence, $m_c = 40$ is the number of modes that can be coupled.

4. Low-Gain Situation

Let

$$a_n = |a_n|e^{i\Phi_n} = const \tag{24}$$

$$a_m = |a_m|e^{i\Phi_m} = const \tag{25}$$

By substituting equations (24) and (25) into (19), we have

$$G = 2Re\frac{\Delta a_n}{a_n} = 2G_0'(\frac{L}{2})^3\sum_{m=1}^{m_c} e^{-(\omega_n-\omega_m)^2\sigma_z^2/2v_z^2}\frac{\omega_m}{\omega_n}F_B(\frac{\omega_m}{\omega_n}\xi)$$

$$\times \frac{|a_m|}{|a_n|}\{\cos(\Phi_m-\Phi_n)[-\frac{2\sin^2(\theta_n-\theta_m)}{\theta_m^2(\theta_n-\theta_m)} + \frac{2\sin^2\theta_n}{\theta_n\theta_m}(\frac{1}{\theta_n}+\frac{1}{\theta_m}) - \frac{2\sin2\theta_n}{\theta_m\theta_n}]$$

$$+ \sin(\Phi_m-\Phi_n)[\frac{sin2(\theta_n-\theta_m)}{\theta_m^2(\theta_n-\theta_m)} - \frac{\sin2\theta_n}{\theta_n\theta_m}(\frac{1}{\theta_n}+\frac{1}{\theta_m}) + \frac{2\cos2\theta_n}{\theta_m\theta_n}]\} \tag{26}$$

$$G_0' = \frac{\omega_b^2 a_w^2 F_B(\xi)(2k_w)}{4c^2\gamma_0^3} \tag{27}$$

$$\theta_n + \frac{L}{2}\Delta k_n \tag{28}$$

$$\theta_m + \frac{L}{2}\Delta k_m \tag{29}$$

(1) Mode-Locking Conditions

$$\begin{cases} \dfrac{(\omega_m-\omega_n)^2\sigma_z^2}{2v_z^2} < 1 \\ \Phi_m = \Phi_n \\ |a_m| \sim |a_n| \\ \theta_m \sim \theta_n(\omega_m \sim \omega_n) \end{cases} \tag{30-1~4}$$

$(n = 1, 2, \cdots, m_c;\quad m = 1, 2, \cdots, m_c)$

Equation (30) indicates that when the phases (and amplitudes) of m_c short-pulse modes of almost the same frequencies are identical, they are coupled into a single optical mode.

(2) Gain of Coupled Mode

Using equation (30) in (26), we have

$$G_c = m_c G_1 \tag{31}$$

$$G_1 = -2G_0 \left(\frac{L_w}{2}\right)^3 \frac{d}{d\theta_n}\left(\frac{\sin^2\theta_n}{\theta_n^2}\right) \tag{32}$$

$$G_0 = \frac{\omega_b^2 a_w^2 F_B^2(\xi)\,(2k_w)}{4c^2\gamma_0^3} \tag{33}$$

(3) Power of Coupled Mode

$$P_c = P_0\,(1 + G_c) = P_0\,(1 + m_c G_1) \tag{34}$$

5. High-Gain Situation

$$a_n = a_{n_0} e^{i\Phi_n z + \alpha_n z} \tag{35}$$

Let

$$a_m = a_{m_0} e^{i\Phi_m z + \alpha_m z} \tag{36}$$

By substituting equations (35) and (36) into (19), we get

$$a_n = \sum_{m=1}^{m_c} \frac{2G_0'(\Delta k_m + \Phi_m)\,\alpha_m}{[(\Delta k_m + \Phi_m)^2 + \alpha_m^2]^2} \frac{a_{m_0}}{a_{n_0}} \frac{\omega_m}{\omega_n} F_B\left(\frac{\omega_m}{\omega_n}\xi\right)$$
$$\times \exp[-(\omega_m - \omega_n)^2\sigma_z^2/2v_z^2] \exp[i(\Delta k_m - \Delta k_n)z + i(\Phi_m - \phi_n)z + (\alpha_m - \alpha_n)z] \tag{37}$$

$$\Phi_n = -\sum_{m=1}^{m_c} \frac{G_0'[(\Delta k_m + \Phi_m)^2 - \alpha_m^2]}{[(\Delta k_m + \Phi_m)^2 + \alpha_m^2]^2} \frac{a_{m_0}}{a_{n_0}} \frac{\omega_m}{\omega_n} F_B\left(\frac{\omega_m}{\omega_n}\xi\right)$$
$$\times \exp[-(\omega_m - \omega_n)^2\sigma_z^2/2v_z^2] \exp[i(\Delta k_m - \Delta k_n)z + i(\Phi_m - \phi_n)z + (\alpha_m - \alpha_n)z] \tag{38}$$

(1) Mode-Locking Condition

$$\begin{cases} \dfrac{(\omega_m - \omega_n)^2\sigma_z^2}{2v_z^2} \ll 1 \\ \Phi_m = \Phi_n \\ a_{m_0} \sim a_{n_0} \\ \alpha_m \sim \alpha_n \\ \Delta k_m \sim \Delta k_n \,(\omega_m \sim \omega_n) \end{cases} \tag{39-1~4}$$

$$(n = 1, 2, \cdots, m_c;\quad m = 1, 2, \cdots, m_c)$$

(2) Gain of Coupled Mode

By applying equations (37) and (38) to (39), we get

$$\alpha_n = \frac{2(m_c G_0)(\Delta k_n + \Phi_n)\alpha_n}{[(\Delta k_n + \Phi_n)^2 + \alpha_n^2]^2} \tag{40}$$

$$\Phi_n = -\frac{(m_c G_0)[(\Delta k_n + \Phi_n)^2 - \alpha_n^2]}{[\Delta k_n + \Phi_n)^2 + \alpha_n^2]^2} \tag{41}$$

From equations (40 and (41), we can obtain the following solutions:

$$\alpha_n = \frac{\sqrt{3}}{2}(m_c G_0)^{1/3}\left[1 - \left(\frac{\Delta k_n}{3(m_c G_0)^{1/3}}\right)^2\right] \tag{42}$$

$$\Phi_n = \frac{1}{2}(m_c G_0)^{1/3}\left[1 - 4\frac{\Delta k_n}{3(m_c G_0)^{1/3}}\right] \tag{43}$$

(3) Power of Coupled Mode

$$P_c = P_0 \exp\left\{\sqrt{3}(m_c G_0)^{1/3} L_w \left[1 - \left(\frac{\Delta k_n}{3(m_c G_0)^{1/3}}\right)^2\right]\right\} \tag{44}$$

III. Conclusions

The gain of the coupled mode of an IR short-pulse FEL was studied and mode-locking conditions (equations (30) and (39)) were obtained. Due to mode coupling, the number of active modes in the cavity is reduced by a factor of m_c and the low gain is increased by a factor of m_c (equation (31)). The exponential growth rate will rise by a factor of $m_c^{1/3}$ (equation (42)); m_c can be determined by equations (20) and (23).

References

1. D. Oepts and W.B. Colson, "Phase Locking in an Infrared Short-Pulse Free Electron Laser," IEEE JOURNAL OF QUANTUM ELECTRONICS, Vol 26 No 24, 1990, p 723.

2. Yu Ming [0060 2404], "General Description of Various FEL Longitudinal Nodes," QIANG JIGUANG YU LIZI SHU [HIGH POWER LASER AND PARTICLE BEAMS], Vol 3 No 2, 1991, p 127.

Effects of Mirror Coating Thickness Nonuniformities on Polarization, Optical Image Properties of Laser, Beacon Light

92FE0442D Chengdu QIANG JIGUANG YU LIZI SHU [HIGH POWER LASER AND PARTICLE BEAMS] in Chinese Vol 4 No 1, Feb 92 pp 59-64

[Article by Xiong Shengming [3574 0524 2494] and Zhang Yundong [1728 0061 3159] of the CAS Institute of Optics and Electronics, P.O. Box 350, Shuangliu, Chengdu 610209: "Effects of Mirror Coating Thickness Nonuniformities on Polarization, Optical Image Properties of Laser, Beacon Light"; MS received 23 Jul 91, revised 20 Sep 91]

[Text] **Abstract**

The distribution of coating thickness across a 0.8-m-diameter mirror is discussed under the geometric constraints of the coating chamber. The effect of nonuniformity of the metal-enhanced high-reflective-index coating on the polarization of the light beam is presented. Phase distortions associated with the 1.06-μm laser and the 0.5893-μm beacon light are calculated. By means of design modification, phase changes of the same sign are obtained to allow the beacon light to achieve its expected objective.

I. Introduction

The diameter of the mirror on the emitting end of a high power laser is D. Consider the light beam following a Gaussian distribution; the angle of divergence at the waist is $\theta \approx \lambda/D$ (where λ is the wavelength of the laser). Furthermore, considering other nonlinear optical effects such as the thermal blooming caused by the transport of high power laser through the atmosphere and excited Raman scattering, the mirror diameter D ought to be large. In practice, the main mirror of a high power laser is usually 5~20 m in diameter. A large diameter is difficult and costly to make. Moreover, the preparation of its coating, especially the uniformity of the coating thickness, is extremely critical and difficult. The nonuniformity causes polarization aberration and wave-front distortion which affect the far-field diffraction characteristics.[1]

Another important issue of a high power laser system is that there are many factors causing wave-front errors in the optical path. The energy of the laser beam is dispersed, which needs to be compensated using the adaptive optical

technique. However, in order to make this kind of correction possible, a suitable light source, usually called the beacon light, is required as the information carrier for the wave-front error.

A phase shift is produced as a light beam is reflected by a coated mirror. Different phase shifts are generated by light of different wavelengths. However, due to nonuniformity of the coating thickness, phase distortions are generated. At different wavelengths, the phase distortions are also different. It is even possible to have phase distortions of opposite signs. Hence, the opposite effect will be produced when it is compensated by the beacon light. Thus, the expected result cannot be achieved.

Based on existing conditions, the coating thickness distribution on a 0.8-m-diameter near-spherical mirror is calculated by taking the geometric constraints of the coating chamber into consideration. Furthermore, this distribution is optimized. The phase distortions produced by this type of metal-enhanced high-reflectance coating series at the laser wavelength, i.e., 1.06 μm, and the beacon light wavelength, i.e., 0.5893 μm, are analyzed. By modifying the design of the coating, the signs of phase distortions at these two wavelengths are consistent.

II. Effect of Physical Constraints in Coating Machine on Coating Uniformity

There are two types of uniformities concerning the coating of a large-diameter mirror, i.e., orientation uniformity and radial uniformity. Orientation uniformity can be easily compensated by spinning the mirror at a high speed via an evaporating ring such as the one shown in Figure 1. Usually, for a large-diameter mirror, from a safety standpoint, a low spin rate is desired; hence, it is necessary to use a ring-shaped vapor source to achieve excellent orientation uniformity. However, radial distribution of coating thickness is more difficult to control. Radial distribution of coating thickness depends upon three parameters[2]: 1) the F value of the mirror and the nonspherical shape of the surface, 2) the distance between the vapor source and the substrate H, and 3) the source offset D from the vapor source to the center of rotation of the mirror D (offset). With a spherical rotation fixture, the coating thickness at an arbitrary point P on the substrate is

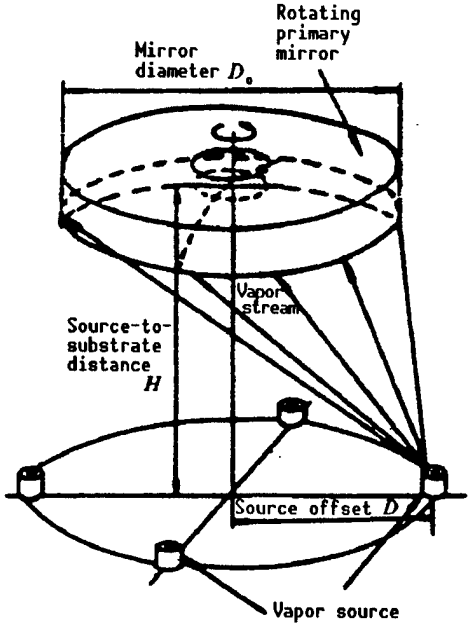

Figure 1. Ring Source Coating Geometry Using Series of Vapor Sources Arranged to Simulate a Ring Vapor Source of Diameter 2D Placed Underneath a Rotating Primary Mirror

$$t_{sp} = \frac{mh}{\mu\pi} \cdot \frac{[(h^2+D^2+\rho^2)(h\cos A+\rho\sin A)-2\rho D^2\sin A]}{[h^2+(D+\rho)^2]^{3/2} \cdot [h^2+(D-\rho)^2]^{3/2}} \quad (1)$$

where

$$h = H - R\ (1 - \cos A) \quad (2)$$

$$\sin A = \frac{\rho}{R} \quad (3)$$

In the above equations, m is the total weight of the evaporated material, μ is its density, R is the radius of the spherical mirror, and ρ is the radial radius from point P to the axis of rotation. The relative thickness is the ratio of t_{sp} to t_{so}, which is the thickness in equation (1) when $\rho = 0$.

Figure 2 shows the optimal condition for an 0.8-m-diameter F/2.0 mirror to achieve coating uniformity. From this figure, one can see that in order to achieve better than 0.5 percent in uniformity, the distance between the vapor source and the substrate needs to be 0.9 m and the offset is 0.63 m. The coating machine should have a height of 1.3 m and a diameter of 1.5 m. However, our equipment does not meet these requirements. Due to cost considerations, modifications will have to be made for the existing equipment. Therefore, it is difficult to achieve the ideal coating uniformity. Figure 3 shows the effect of offset D on the coating uniformity at a known height H. From the figure, when H is 0.65 m, the offset should be 0.48~0.5 m to achieve a uniformity of ±1.5 percent. Nevertheless, the diameter of our existing coating machine is 1.2 m and the maximum offset one can attain is 0.46 m. Figure 4 shows the coating thickness as a function of height with a bias of 0.45 m. This figure shows that a ±2 percent uniformity may be obtained at a height of 0.56~0.64 m.

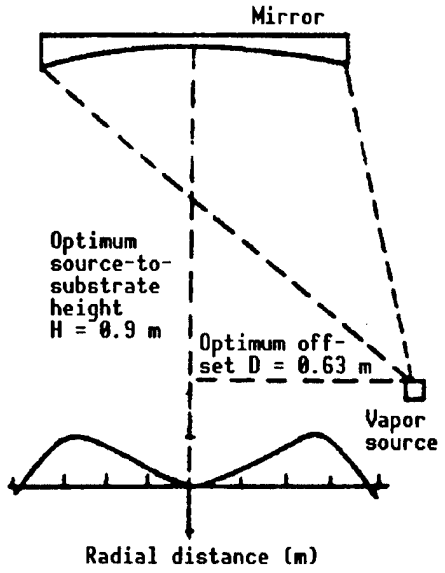

Figure 2. Optimized Coating Thickness Uniformity for 0.8-m-Diameter F/2.0 Concave Mirror

In the above discussion, shields are not used. In all uniformity calculations, all vapor sources are small-area sources and obey the cosine distribution. The mirror is considered to be spherical.

III. Initial Design of Coating Series

The main laser wavelength is selected at near 1 μm, e.g., 1.06 μm. The beacon light might either be scattered laser light reflected by the target or a laser light of another wavelength on a relay satellite. We are using the artificial beacon light produced by the resonant scattering of sodium atoms in the alkali metal layer formed by falling meteorites 80~100 km high in the atmosphere in response to an 0.5893 μm laser as proposed by French astronomer Labyrie. It is

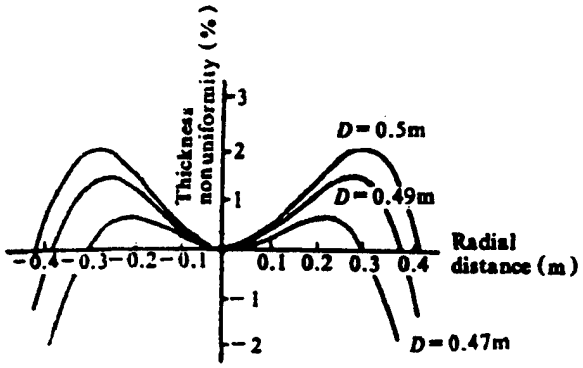

Figure 3. Coating Thickness Nonuniformity for 0.8-m-Diameter F/2.0 Concave Mirror for Various Offset Distance and for a Fixed Source-to-Substrate Distance of 0.65 m

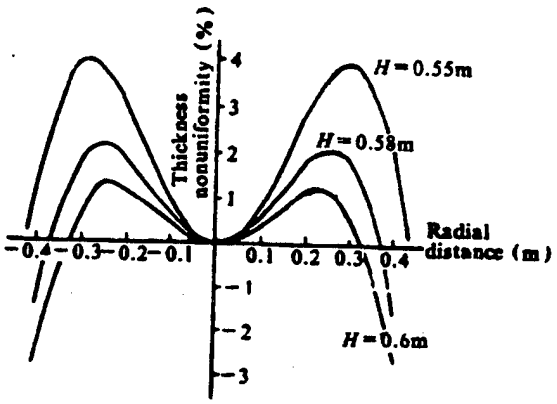

Figure 4. Coating Thickness Nonuniformity for 0.8-m-Diameter F/2.0 Concave Mirror for Various Height and a Fixed Offset Distance of 0.45 m

assumed that a reflectance of greater than 99 percent is required at 1.06 μm and that at 0.5893 μm it needs to be higher than 95 percent.

The initial design of the coating is

$$G/Cr/Ag/Al_2O_3/(LH)^2/Air$$

where L and H are the one-fourth-wavelength thicknesses of SiO_2 and Ta_2O_5 at the laser wavelength, respectively. Cr and Al_2O_3 are bonding layers. G is the substrate and the geometric thickness of the Ag layer is 70 nm.

The design with a full or half one-fourth-wavelength dielectric film on a metal layer is selected because it is easy to monitor. Initially, the $(LH)^2$ structure was chosen because it has wide bands of reflectance near the two wavelengths of interest. Ag was selected because it has a high reflectance band ranging from visible to infrared. Based on this design, the maximum incident angle of the main mirror is 15°. The following is a discussion of the effect of coating nonuniformity on the polarization characteristics (ellipticity and phase distortion) at the two wavelengths of interest.

IV. Effect of Thickness Nonuniformity on Ellipticity of the Initial Coating Design

When a linearly polarized light shines on the main mirror at an oblique angle, the reflected light is elliptically polarized. In other words, there is a phase difference between the vector component P which is parallel to the incident plane and the vector S which is perpendicular to the incident plane. Furthermore, the perpendicular components have different amplitudes. Figure 5 shows the changes in reflectivity and phase as a function of thickness nonuniformity at the main laser wavelength and beacon light wavelength. At 1.06 μm, the phase difference $\Delta p - \Delta s < 1°$. Even with a 4 percent thickness nonuniformity, the difference in reflectivity is less than 0.02 percent.

At 0.5893 μm, the phase difference is less than 3.5° and the reflectivity difference is less than 0.2 percent. In conclusion, at an incident angle of 15°, the reflected light is elliptically polarized in a very flat manner. A 4-percent thickness nonuniformity has very little impact on its ellipticity.

V. Effect of Coating Nonuniformity on Phase Distortion of Reflected Waves at Different Wavelengths

The characteristics of nonuniformity of thin coating include different optical thicknesses and phase shifts (phase distortions). Phase shift will cause image distortion. In particular, it significantly affects the far-field diffraction characteristics of the system. Figure 6 shows the phase distortions of the reflected waves at the two wavelengths of interest as a function of coating thickness nonuniformity for the initial design. As one can see, at 1.06 μm, a +4 percent nonuniformity only results in an −11° phase shift or a wave-front distortion of −λ/32.7. A 1-percent nonuniformity causes a phase shift of −2.4° or a wave-front distortion of λ/150. At 0.5893 μm, the phase distortion is larger. A +4-percent nonuniformity results in a phase shift of 140.28° or a wave-front distortion of λ/2.57. A 1-percent nonuniformity causes a phase shift of −8.5° or a wave-front distortion of λ/42.3.

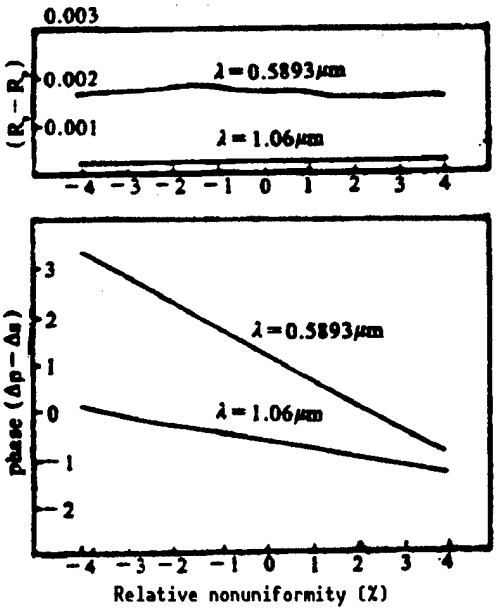

Figure 5. Maximum Difference in p and s Components of Reflectivity and Phase for Initial Selected Design as a Function of Thickness Nonuniformity for 15° Incidence Angle

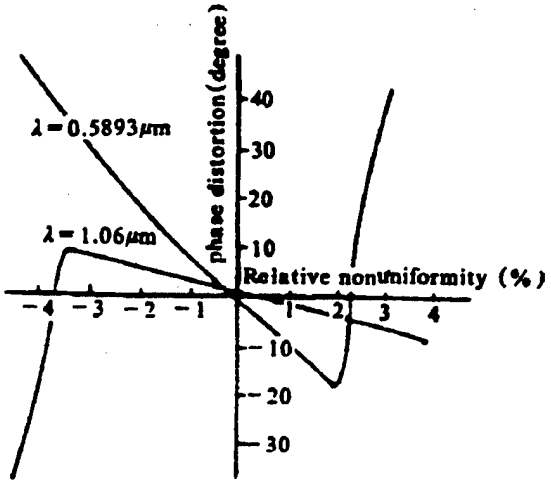

Figure 6. Phase Distortion in Degrees for the Initial Selected Design at the Two Wavelengths as a Function of Thickness Nonuniformity for 0.8-m-Distance F/2.0 Mirror

Figure 7 shows the radial distribution of phase distortion at the wavelengths of interest for an 0.8-m-diameter, F/2.0 mirror. The calculation is based on an assumption that the large mirror surface is close to spherical. The distance between the vapor source and the substrate is 0.55 m and the offset is 0.45 m.

Opposite phase distortion signs cause other problems as well. An optically erroneous image at the wavelength may be partially corrected by means of self-adaptive optical compensation. If the wave-front distortion of another

wavelength has the opposite sign, the correction at one wavelength will cause the further deterioration of the wave front at the other wavelength. In order to simultaneously correct the wave fronts at two wavelengths, phase distortions at these two wavelengths ought to have the same sign. To the extent possible, the phase distortions of these two wavelengths must be consistent. To this end, a modified design was adopted.

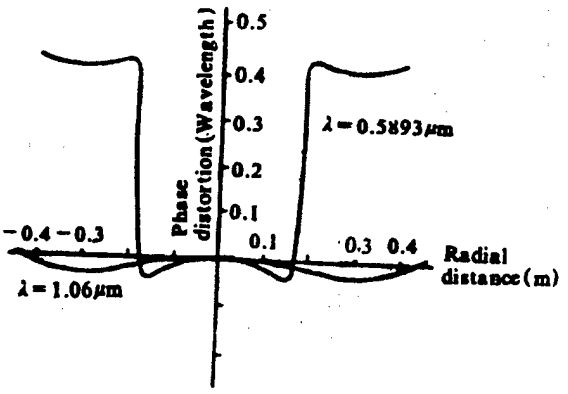

Figure 7. Phase Distortion for Initial Selected Design Along the Radial Distance of 0.8-m-Diameter F/2.0 Mirror for Source-to-Substrate Height of 0.55 m and Offset Diameter of 0.45 m

VI. Modified Design and Its Effect on Polarization and Phase Distortion

To have the same phase distortion signs, numerous simple designs were investigated. Based on theoretical calculation, the modified coating was designed as follows:

$$G/Al_2O_3/Ag/Al_2O_3/(LH)^2\frac{H}{2}/Air$$

H and L are the one-fourth-wavelength Ta_2O_5 and SiO_2 correction coatings for 1.17 μm, respectively, and Al_2O_3 is the bonding layer. The effect of thickness nonuniformity on the polarization characteristics of this modified design is shown in Figure 8. It was found that the reflectivity of this design varies significantly with thickness nonuniformity at an 0.5893-μm wavelength. The two designs have comparable reflectivities at 1.06 μm. Compared to the initial design, the reflectivity of the modified design is slightly higher than a +4-percent nonuniformity. At 0.5893 μm, the reflectivity of the modified design is lower than that of the initial design. Figure 9 shows the phase distortions produced by the modified design at two wavelengths. It shows that a 4-percent nonuniformity results in a −23° phase shift, or a λ/15.6 wave-front distortion, at 1.06 μm. A 1-percent nonuniformity causes a phase shift of −4.5° or a λ/80 wave-front distortion. At 0.5893 μm, the distortion is larger: a 4-percent nonuniformity produces a −55° phase shift, or a λ/6.5 wave-front distortion and a

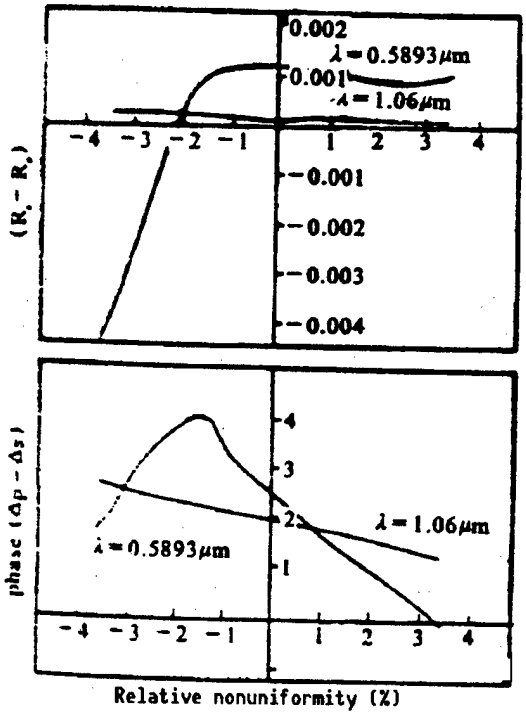

Figure 8. Maximum Difference in p and s Components of Reflectivity and Phase for Modified Design as a Function of Thickness Nonuniformity for 15° Incidence Angle

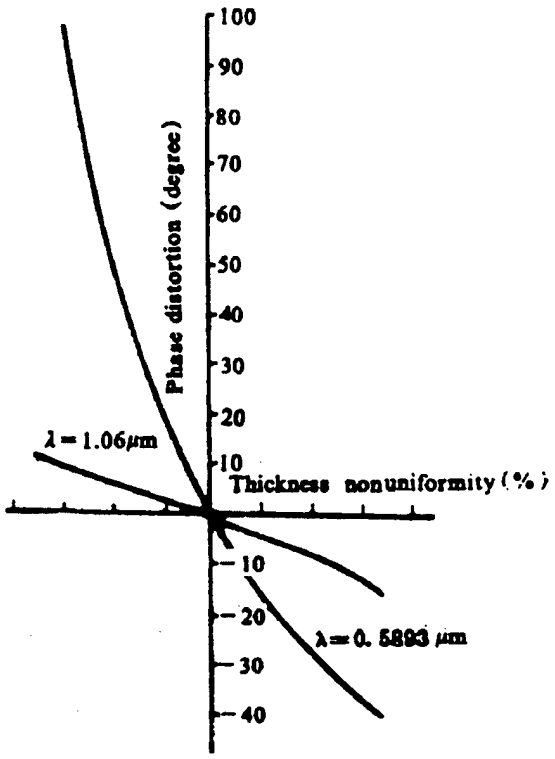

Figure 9. Phase Distortion in Degrees for the Modified Design at the Two Wavelengths as a Function of Thickness Nonuniformity for 0.8-m-Diameter F/2.0 Mirror

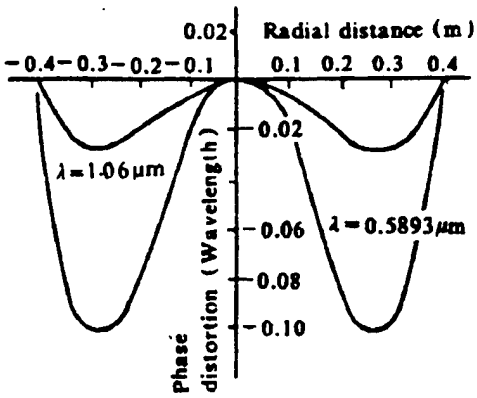

Figure 10. Phase Distortion for Modified Design Along Radial Distance of 0.8-m-Diameter F/2.0 Mirror for Source-to-Substrate Height 0.56 m and Offset Distance of 0.45 m

1-percent nonuniformity results in a $-14.5°$ phase shift, or a $\lambda/24.8$ wave-front distortion. The wave-front distortions corresponding to different coating thickness nonuniformities have identical signs at these two wavelengths.

Figure 10 shows the radial distribution of phase distortion for the modified design at the two wavelengths for the 0.8-m F/2.0 mirror.

VII. Conclusions

The analysis described above indicates that when using the modified design (adding one-fourth- or one-eighth-wavelength dielectric coatings on top of metallic silver), coating thickness nonuniformity could produce the same phase distortion signs at two wavelengths. At an incident angle of 15°, the modified design does not have much impact on its polarization characteristics. The reflectivity in the wavelength range of interest does not decrease. This is a suitable design for an 0.8-m-diameter mirror. For ease of monitoring, all dielectric coating was controlled by a single wavelength to minimize any variation caused by dispersion due to the use of different wavelengths for controlling different layers.

References

1. T.P. Washburne, M.J. Konopniki, and T.D. Miller, SPIE, Vol 1166, 1989, p 340.

2. Tang Jinfa [0781 2516 4099] and Gu Peifu [7357 1041 1133], "Thin-Film Optics and Technology," Machinery Industry Publ. House, 1989.

Effects of Phasing Errors on Beam Combining

92FE0442E Chengdu QIANG JIGUANG YU LIZI SHU [HIGH POWER LASER AND PARTICLE BEAMS] in Chinese Vol 4 No 1, Feb 92 pp 65-70

[Article by Hu Zhiping [5170 1807 1627], Yue Shixiao [2867 2514 0879], and Song Ruhua [1345 1172 5478] of the University of Electronic Science and Technology (UEST) of China, Chengdu 610054, and Zhou Hongyang [0719 4767 7122] of the Institute of Computer Applications, China Academy of Engineering Physics, P.O. Box 532, Chengdu 610003: "Effects of Phasing Errors on Beam Combining"; MS received 10 Apr 91, revised 16 Sep 91, supported by a grant from the National High-Technology Foundation. See also JPRS-CST-92-013, 29 Jun 92 pp 58-59.]

[Text] **Abstract**

On the basis of work done on vacuum synthetic-aperture beam control, the effect of phase control errors (including tilt, piston, and focus errors) on coherent beam combination is analyzed and discussed. A corresponding physical model is presented. In addition, numerical computation was done and is illustrated in the form of three-dimensional plots.

I. Introduction

The use of a synthetic aperture as a coherent high-power laser emission system has attracted a great deal of interest in recent years.[1] By controlling the wave-front phase of the light beams from each subaperture of the synthetic aperture system, it is possible to achieve coherent combination of the light beams in the far field. Nevertheless, phase-control errors usually occur with wave-front phase control. There are several factors affecting the control of phase which leads to a decline in performance of the synthetic aperture system and lowers the far-field peak of the combined beam. We have studied the beam-control concept under ideal conditions (i.e., without various factors affecting the precise phase control of the beam). A physical model for the alignment, transition and coherent and noncoherent combination of the beams was presented. Furthermore, theoretical analysis and numerical computation were performed.[2,3] On the basis of our previous work, this paper discusses factors affecting the precision of phase control (e.g., piston error, tilt error, and focus error) and their effect on coherent beam combination.

A physical model is presented and numerical computation is carried out; results are illustrated in the form of three-dimensional figures.

II. Theoretical Analysis and Numerical Computation

To facilitate the theoretical analysis, let us assume that the laser emits a planar beam.

$$U_0(x_1, y_1) = Bp_1(x_1, y_1) \tag{1}$$

where B is a constant which is there for use in the analysis to follow. Let B = 1 at this point; $p_1(x_1, y_1)$ is the pupil of the light emission system which is defined as follows:

$$p_1(x_1, y_1) = \begin{cases} 1 & x_1^2+y_1^2 \le (d/2)^2 \\ 0 & (x_1^2+y_1^2) > (d/2)^2 \end{cases} \tag{2}$$

where d is the diameter of the pupil.

Let us assume that the synthetic aperture is composed of N = 1 x m apertures and the center coordinate of each aperture is $x_s(i,j)$, $y_s(i,j)$, and $i=1,2,\cdots,1$ and $j=1,2,\cdots,m$. The coherent combined far field is[2]:

$$\begin{aligned} U(x,y) &= A(x,y,z)F\{\sum_{i=1}^{1}\sum_{j=1}^{m} p_1(r_{1ij})\}\Big|_{(y-y_t)/\lambda z}^{(x-x_t)/\lambda z} \\ &= A(x,y,z)F\{p_1(r_1)\}\Big|_{(y-y_t)/\lambda z}^{(x-x_t)/\lambda z} \\ &\quad \cdot \sum_{i=1}^{1}\sum_{j=1}^{m} \exp\{-2\pi j[\frac{x-x_t}{\lambda z}x_s(i,j) + \frac{y-y_t}{\lambda z}y_s(i,j)]\} \end{aligned}$$

where $A(x,y,z) = \exp(jkz) \cdot \exp[(\frac{jk}{2z})(x^2+y^2)]/(j\lambda z)$, $F\{\ \}$ represents the Fourier transform, $k = 2\pi/\lambda$ where λ is the wavelength, and (x_t, y_t) is the coordinate of the target. Let $x_t = y_t = 0$ (i.e., all the beams from the subapertures converge on the axial axis), then we have

$$\begin{aligned} U(x,y) &= A(x,y,z)F\{p_1(r_1)\}\Big|_{y/\lambda z}^{x/\lambda z} \\ &\quad \cdot \sum_{i=1}^{1}\sum_{j=1}^{m} \exp\{-2\pi j[\frac{x}{\lambda z}x_s(i,j) + \frac{y}{\lambda z}y_s(i,j)]\} \end{aligned} \tag{3}$$

Obviously, from equation (3), the peak light intensity of the coherently combined beam is:

$$I_M = |U(0,0)|^2 = \frac{1}{\lambda^2 z^2}|F\{p_1(r_1)\}|^2 \cdot (1xm)^2 = N^2 \cdot I_{1M} \tag{4}$$

where I_{1M} is the peak intensity of each individual subaperture system at (0,0,z).

In the following analysis and computation, let N = 16, d = 1m, λ = 1 μm, z = 10^3km.

Figure 1 shows the intensity distribution of the coherent combination of beams by the synthetic aperture. (The numbers shown are relative values.) Figure 2 shows the energy distribution curve in the far field; R_0 represents the Airy disc radius: E(AIRY DISC)/E(TOTAL) = 0.868299E+00 indicates that the energy in the first airy disc is 86.8299 percent of the total energy. R_0 = 0.61 x λ x z/b, which is in units of 0.61 x λ z/b where λ is the wavelength, z is the distance from the mirror to the target, and b is the effective pupil radius of the phase-control array.

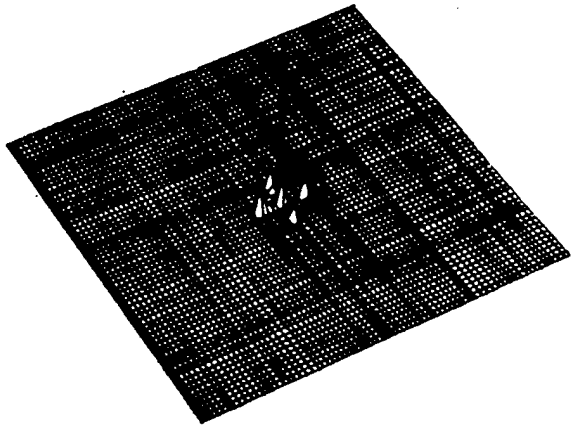

Figure 1. The Intensity Distribution of Coherent Beam Combination

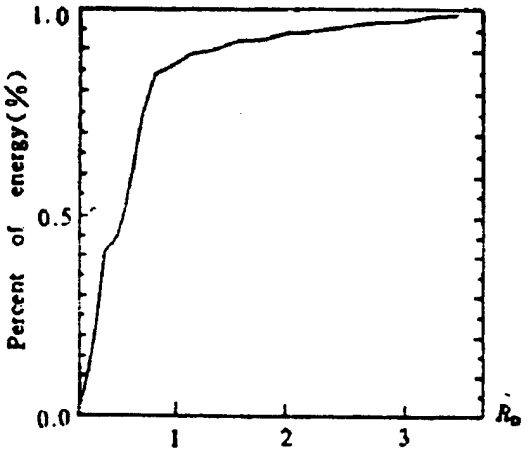

E(AIRY DISC)/E(TOTAL) = 86.8 %

Figure 2. The Regional Energy Distribution in the Far Field. E = 86.8%

1. Effect of Piston Error in Phase Adjustment[4]

When performing wave-front phase adjustment and control of a divergent beam from a subaperture, a phase error in the form of exp ($jk\varphi_{ij}$), where φ_{ij} is independent of x_1 and y_1, is the piston error. Hence, the synthetically combined far-field distribution becomes:

$$U_p(x,y) = A(x,y,z)\,F\{p_1(r_1)\}\Big|_{y/\lambda z}^{x/\lambda z} \cdot \sum_{i=1}^{l}\sum_{j=1}^{m} \exp\left[-2\pi j\left(\frac{x}{\lambda z}x_s(i,j) + \frac{y}{\lambda z}y_s(i,j)\right)\right] \cdot \exp(jk\varphi_{ij}) \tag{5}$$

Consequently, the coherently synthesized peak intensity is

$$I_{M_p} = |U_p(0,0)|^2 = \frac{1}{\lambda^2 z^2}\left|F\{p_1(r_1)\}\Big|_0^0\right|^2 \cdot \sum_{i=1}^{l}\sum_{j=1}^{m}\exp(jk\varphi_{ij})\Bigg|^2 \tag{6}$$

In general, $\left|\sum_{i=1}^{l}\sum_{j=1}^{m}\exp(jk\varphi_{ij})\right|^2 \le N^2$,

Therefore, $I_{MP} \le N^2 \cdot I_{1M}$

This means that the piston error would cause the peak intensity to fall.

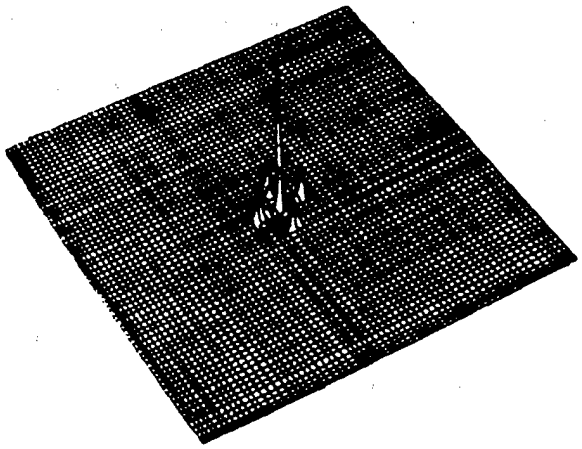

Figure 3. The Intensity Distribution With the Piston Errors
($\varphi_{11}=\varphi_{12}=\varphi_{21}=\varphi_{22}=0.5\lambda$, other $\varphi_{ij}=0$)

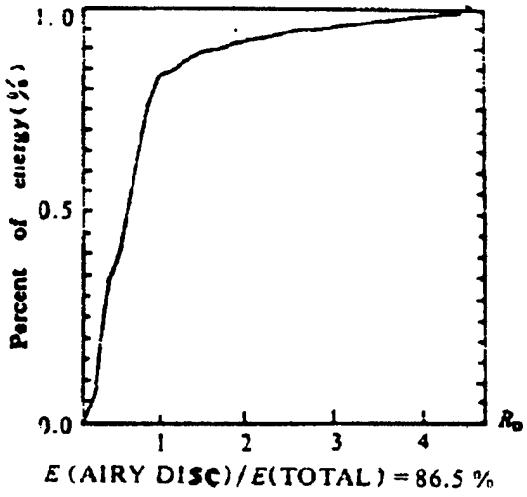

E(AIRY DISC)/E(TOTAL) = 86.5 %

Figure 4. The Regional Energy Distribution in the Far Field With the Piston Errors
($\varphi_{11}=\varphi_{12}=\varphi_{21}=\varphi_{22}=0.5\lambda$, other $\varphi_{ij}=0$), E=86.5%

Figures 3 and 4 show the far-field light intensity distribution and energy distribution, respectively, with $\varphi_{11} = \varphi_{12} = \varphi_{21} = \varphi_{22} = 0.5\ \lambda$ and $\varphi_{ij} = 0$. These figures show that piston error will lead to a decline of the peak intensity of the combined beam. However, it has a relatively small effect on the energy in the first Airy disc.

2. Effect of Tilt Error[4]

A tilt error is a phase error term in the form of $\exp([jk[c_{ijx}(x-x_s(i,j)) + c_{ijy}(y-y_s(i,j))]]$ which is caused by the tilt and vibration of the subaperture. In this case, the optical field of the combined beam can be expressed as follows:

$$
\begin{aligned}
U_T(x,y) &= A(x,y,z,)\sum_{i=1}^{l}\sum_{j=1}^{m} F\{p_1(r_{1ij})\cdot\exp[jkc_{ijx}(x_1-x_s)+jkc_{ijy}(y_1-y_s)]\}\Big|_{y/\lambda z}^{x/\lambda z} \\
&= A(x,y,z,)\sum_{i=1}^{l}\sum_{j=1}^{m} F\{p_1(r_1)\exp[jk(c_{ijx}x_1+c_{ijy}y_1)]\}\Big|_{y/\lambda z}^{x/\lambda z} \\
&\cdot\exp\left[-2\pi j\left(\frac{x}{\lambda z}x_s+\frac{y}{\lambda z}y_s\right)\right] \\
&= A(x,y,z)\sum_{i=1}^{l}\sum_{j=1}^{m} F\{p_1(r_1)\}\Big|_{(x-c_{ijy}z)/\lambda z}^{(x-c_{ijx}z)/\lambda z} \\
&\cdot\exp\left[-2\pi j\left(\frac{x}{\lambda z}x_s(i,j)+\frac{y}{\lambda z}y_s(i,j)\right)\right]
\end{aligned}
\qquad (7)
$$

It is obvious that the peak intensity becomes

$$I_{MT} = |U_T(0,0)|^2$$

$$= \frac{1}{\lambda^2 Z^2}\left|\sum_{i=1}^{l}\sum_{j=1}^{m} F\{p_1(r_1)\}\Big|_{-c_{ijy}/\lambda}^{-c_{ijx}/\lambda}\right|^2 \le \frac{1}{\lambda^2 Z^2}\left|\sum_{i=1}^{l}\sum_{j=1}^{m} F\{p_1(r_1)\}\Big|_{0}^{0}\right|^2 = N^2 I_{1M} \tag{8}$$

Figures 5 and 6 are the intensity and energy distribution when $c_{ijx} = c_{ijy} = 0.5 \times 10^{-6}$rad. Based on these figures, we can see that tilt error not only causes the far-field peak light intensity to fall but also results in a reduction of energy in the first Airy disc. The larger the tilt error, the more apparent this effect.

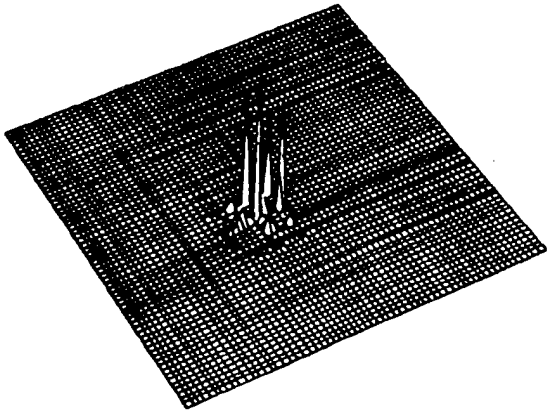

Figure 5. The Intensity Distribution With the Tilt Errors. ($c_{ijx} = c_{ijy} = 0.5 \times 10^{-6}$rad)

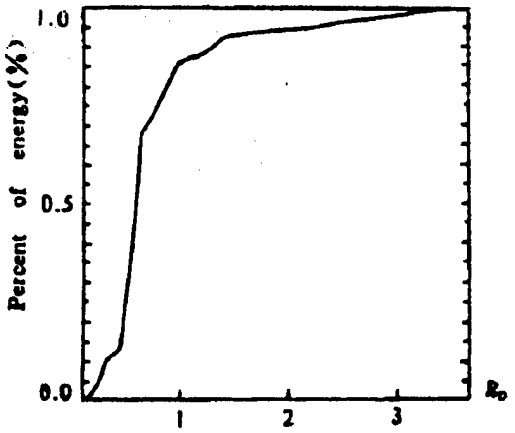

E(AIRY DISC)/E(TOTAL) = 85.6 %

Figure 6. The Regional Energy Distribution in the Far Field With the Tilt Errors ($c_{ijx} = c_{ijy} = 0.5 \times 10^{-6}$rad), E = 85.6%

3. Effect of Focus Error

When focusing the beam, if it is not accurately focused, a focus error term such as the following will be introduced[5]:

$$\exp\{jk\epsilon_{ij}[x_1 - x_s(i,j))^2 + (y_1 - y_s(i,j))^2]/2\}$$

Hence, the far-field combined beam becomes:

$$U_F(x,y) = A(x,y,z)\sum_{i=1}^{l}\sum_{j=1}^{m} F\{p_1(r_{1ij})\cdot\exp[jke_{ij}((x_1-x_s)^2+(y_1-y_s)^2)/2]\}\Big|_{y/\lambda z}^{x/\lambda z}$$

$$= A(x,y,z)\sum_{i=1}^{l}\sum_{j=1}^{m} F\{p_1(r_1)\exp(jke_{ij}r_1^2/2)\}\Big|_{y/\lambda z}^{x/\lambda z}$$

$$\cdot\exp\{-2\pi j[\frac{x}{\lambda z}x_s(i,j) + \frac{y}{\lambda z}y_s(i,j)]\}$$

Let $\epsilon_{ij} = \Delta_{ij}/z$, then

$$U_F(x,y) = A(x,y,z)\sum_{i=1}^{l}\sum_{j=1}^{m}\{p_1(r_1)\exp(jk\Delta_{ij}r_1^2/2z)\}\Big|_{y/\lambda z}^{x/\lambda z}$$

$$\cdot\exp\{-2\pi j[\frac{x}{\lambda z}x_s(i,j) + \frac{y}{\lambda z}y_s(i,j)]\} \tag{9}$$

Hence, the peak intensity of the combined beam is

$$I_{MF} = |U_F(0,0)|^2 = \frac{1}{\lambda^2 Z^2}\left|\sum_{i=1}^{l}\sum_{j=1}^{m} F\{p_1(r_1)\exp(j\pi\Delta_{ij}r_1^2/\lambda z)\}\right|_{0}^{2}_{0}$$
$$\leq \frac{1}{\lambda^2 Z^2}\left|\sum_{i=1}^{l}\sum_{j=1}^{m} F\{p_1(r_1)\}\right|_{0}^{2}_{0} = N^2 I_{1M} \qquad (10)$$

Figure 7 is the intensity distribution of the coherently combined beam at z = 5 x 10^4m without any focus error (Δ_{ij} = 0). Figure 8 shows the intensity distribution at z = 5 x 10^4m with a focus error, i.e., $\Delta_{11} = \Delta_{12} = \Delta_{21} = \Delta_{22} = \Delta_{31} = \Delta_{32} = \Delta_{41} = \Delta_{42} = 0.1$ and $\Delta_{13} = \Delta_{14} = \Delta_{23} = \Delta_{24} = \Delta_{33} = \Delta_{34} = \Delta_{43} = \Delta_{44} = -0.1$; the physical significance is that some of the subapertures are focused in front of the common target and others are behind it. It is apparent that the peak intensity drops considerably in this case. Moreover, the larger the focus error, the more severe the impact on the beam combination.

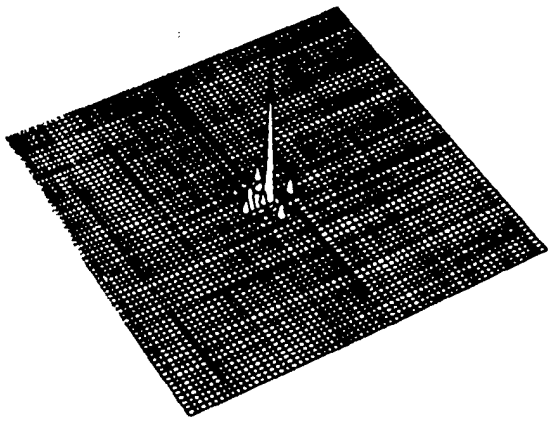

Figure 7. The Intensity Distribution of Coherent Beam Combination Without Focus Errors. ($\Delta_{ij}=0$), $z=5\times10^4$ m.

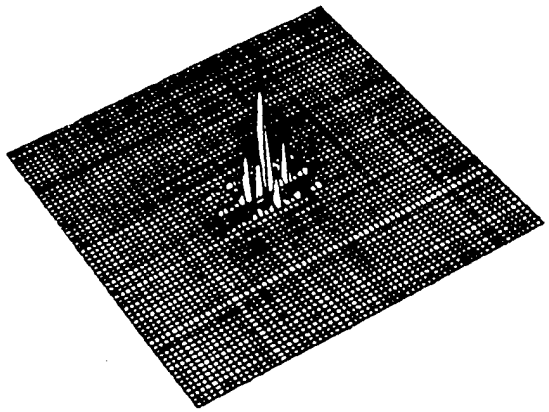

Figure 8. The Intensity Distribution With the Focus Errors ($\Delta_{11}=\Delta_{12}=\Delta_{21}=\Delta_{22}=\Delta_{31}=\Delta_{32}=\Delta_{41}=\Delta_{42}=0.1$, $\Delta_{13}=\Delta_{14}=\Delta_{23}=\Delta_{24}=\Delta_{33}=\Delta_{34}=\Delta_{43}=\Delta_{44}=-0.1$), $z=5\times10^4$ m.

III. Conclusions

A detailed analysis has been done on factors affecting the accurate control of the phase of beam combination by means of a synthetic aperture; furthermore, numerical computation has been done. The results show that the peak intensity of the combined beam drops considerably because of failure of accurate phase control. However, it should be pointed out that the factors considered in the analysis were assumed to be static, instead of random and dynamic variables. As for laser transport in the atmosphere, it is more meaningful to investigate the effects of random and dynamic variables, such as turbulence, on the accuracy of phase control. We plan to work in this area in order to establish a realistic model to study the effect of turbulence on phase-control accuracy.

Acknowledgment

Numerical computation and figure plotting were done with the support and assistance of the Institute of Computer Applications of the China Academy of Engineering Physics.

References

1. J.S. Fender, "Synthetic Aperture Systems," PROC. SPIE, 1983, p 440.

2. Hu Zhiping, et al., "Demonstration of Physical Model and Computer Simulation of Plane-Wave Beam Control," DIANZI KEJI DAXUE XUEBAO [JOURNAL OF UEST OF CHINA], Vol 18 No 5, 1989, p 462.

3. Hu Zhiping, et al., "Beam Control In Multiple Aperture Transmitting Systems," PROC. SPIE, 1990, p 1221.

4. R.R. Butts, "Effects of Piston and Tilt Errors on the Performance of Multiple Mirror Telescopes," PROC. SPIE, 1981, p 293.

5. J.W. Goodman, "Introduction to Fourier Optics," Chapter 6, Section 7, Science Publishing House, Beijing, 1979.

Experimental Research on Velvet Cathodes

92FE0442F Chengdu QIANG JIGUANG YU LIZI SHU [HIGH POWER LASER AND PARTICLE BEAMS] in Chinese Vol 4 No 1, Feb 92 pp 107-113

[Article by Zhang Qi [1728 1142] of the CAS Institute of Electronics, P.O. Box 2702, Beijing 100080, Xing Da [6717 6671] of the Institute of Optoelectronics, Harbin Institute of Technology, and Ken-ichi Ueda and Hiroshi Takuma of the Institute for Laser Science, University of Electro-Communications, Chofushi, Tokyo 182, Japan: "Experimental Research on Velvet Cathodes"; MS received 18 Mar 91, revised 19 Jul 91]

[Text] **Abstract**

The emission characteristics of velvet cathodes have been experimentally studied under long (50~100 ns) and short (3 ns) pulse conditions with corresponding cathode densities of 400 A/cm^2 and 7 kA/cm^2, respectively.

The current-voltage curve was measured. The cathode emission pattern was obtained using the Cerenkov effect. Scanning electron micrographs of the velvet cathode were obtained and the experimental structure of the velvet cathode was measured. The emission mechanism of the velvet cathode is discussed.

I. Introduction

An intense relativistic electron beam (IREB) has a very high current density and a very low temperature. It is a prerequisite for a number of devices such as electron-beam-pumped excimer lasers and FELs. Different applications have different characteristic requirements for the e-beam. An e-beam-pumped excimer laser requires a beam with very good uniformity and the plasma between the anode and cathode should have a low closure speed. A Raman FEL, on the other hand, requires a high brightness and low emissivity.

These requirements can be met by using different diodes and cathode materials. Recently, it was proven that velvet is an excellent cold-cathode material.[1] Its major advantages are as follows: First, its start-up time is very short,[2] i.e., its impedance can drop from infinity to its characteristic value instantaneously. Second, the anode-cathode plasma closure speed is very slow and

plasma expansion is almost unnoticeable. Thus, the current profile of a diode with a velvet cathode is almost an ideal square wave. Third, compared to other cold-cathode materials, the velvet cathode is several orders of magnitude higher in brightness.

However, the emission mechanism of the velvet cathode is still not well understood. To this end, some experimental work is done in order to study the emission mechanism involved.

II. Experimental Apparatus and Results

In this experimental work, three different IREB accelerators are used; their pulse widths are 120 ns, 50 ns, and 3 ns. The 3-ns device is called the Febetron 706. They are essentially composed of three parts: 1) An energy storage unit, which is a Marx generator for the 120-ns and 3-ns apparatus. The 50-ns apparatus uses a high-voltage transformer as its energy storage unit. 2) A pulse formation line, which is a water Blumlein line for the longer-pulse apparatus and an oil-based Blumlein line for the Febetron 706. 3) A diode which has a rectangular e-beam cross section for the longer-pulse apparatus and a circular e-beam cross section for the short-pulse device. The characteristics of these IREB accelerators are tabulated in Table 1.

Table 1. Specifications of the IREB Accelerator Systems

Model / Parameters	IREB source (I)	IREB source (II)	Febetron 706
Output voltage (kV)	300	250	600
Output current (kA)	30	25	6
Output impedance (Ω)	10	10	100
Pulse width (ns)	120	50	3
The shape and area of cathode	Rectangular 40 x 40 cm	Rectangular 20 x 3 cm	Circular ϕ9 mm

The results are as follows.

1. Measuring Cathode Emission Pattern Using Cerenkov Effect

Real-time measurement of the e-beam current was measured by means of Cerenkov radiation using an optical fiber or a quartz plate.[3] This measurement is real-time and is not susceptible to interference.

This experiment was carried out using IREB accelerator (II). The experimental set-up is shown in Figure 1. Figure 2 [photograph not reproduced] depicts the emission pattern of the velvet cathode. It clearly shows that the velvet

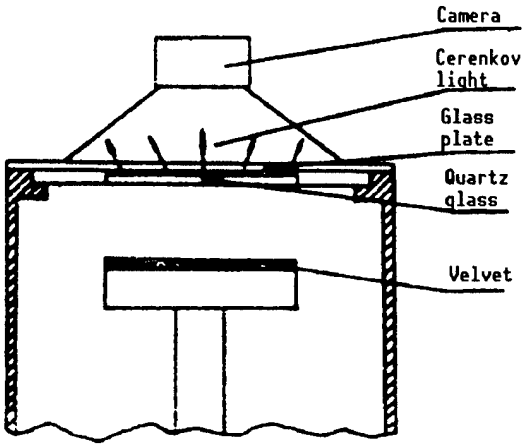

Figure 1. Schematic of Experimental Arrangement

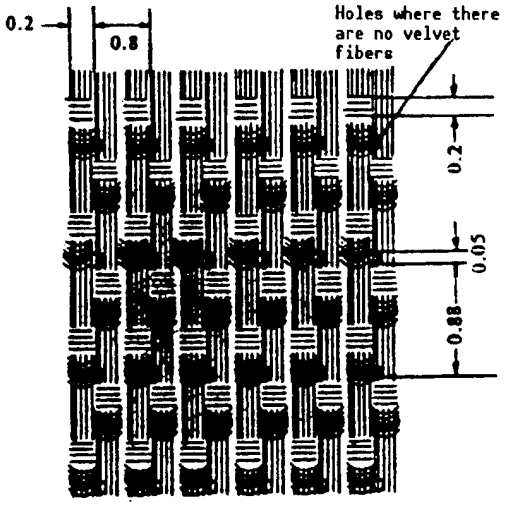

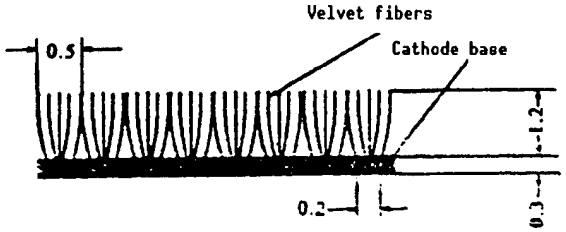

Figure 3. Practical Construction of Velvet Cathode (Unit: mm)

cathode emission is more uniform. Its emission pattern consists of a number of bright and dark spots. The sizes and locations of these points seem to follow a certain pattern.

The structure of the velvet cathode was observed using a microscope and is illustrated in Figure 3. The velvet fibers are essentially standing straight, and are approximately 20 μm in diameter. There are a number of gaps at the back side of the velvet cathode and the sizes and locations of these gaps also follow a certain pattern. We measured the sizes of all the bright and dark spots. They are essentially consistent with the sizes of the velvet cathodes.

2. Recording Time-Integral Current Density Distribution Using a 1-mm-Diameter-Aperture Faraday Cup

This measurement was done on the short-pulse Febetron 706 system, whose cathode is circular. Figure 4 shows its relative current density distribution. From this current density distribution, one can see some small nonuniformity. The current density at the center of the cathode is smaller than that at the edge. The peaks on both sides correspond to the 9-mm diameter which serves as a measurement of the effective cathode size.

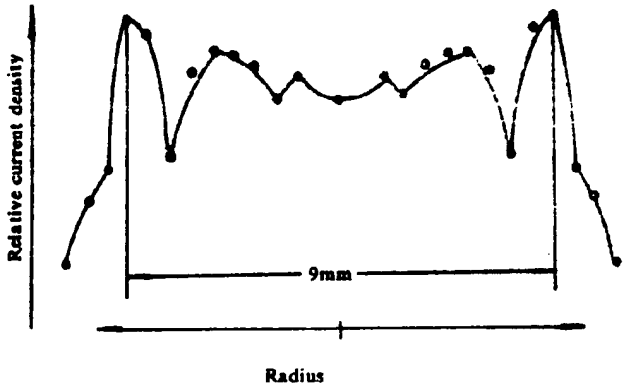

Figure 4. Relative Current Density Profile Obtained by Smaller-Aperture Faraday Cup

3. Scanning Electron Micrographs of the Velvet Fibers After 1,000 Runs, Shown in Figure 5 [Photograph not reproduced]

From the photographs, it is apparent that the tip of the fiber has melted. Its surface is relatively smooth and has been stretched. Another unique feature is that the velvet fibers become brittle after the experiment. They break off easily because they have been carbonized. However, they have not yet become conductors.

III. Discussion of Results

There are two theories that might be used to interpret the emission mechanism of the velvet cathode. One is that it is similar to an explosive emission cathode. We believe that it might explain the mechanism in our experiment with longer pulses (>50 ns) because the electric field strength on the velvet is below 10^5V/cm, which is the low-field case. Hence, electrons are initially emitted from the tip of the fiber. Since the velvet is an insulator, the tip becomes charged after emission.

For an explosive cathode, once the applied voltage exceeds the breakdown voltage, the tips begin to explode. This moment is a function of the applied voltage and the cathode material and is called the breakdown delay time. In the early stage of discovery, the breakdown delay times for a number of materials were quantitatively measured. Russian scientists have done a great deal of work in this area and the values are shown in Figure 6.[4] The breakdown delay time is the time after a pulse voltage is applied to a planar electrode to the formation of a flash point. Recently, we measured the breakdown delay times of velvet at different applied voltages and the results are also included in Figure 6.

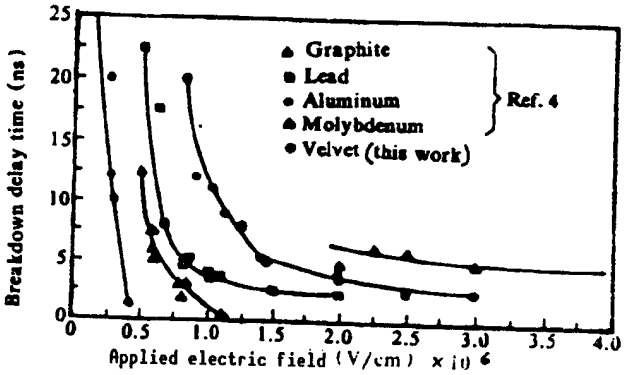

Figure 6. Experimental Breakdown Delay Time as a Function of Applied Field and Electrode Materials

For most emission materials, the following equation[5] applies:

$$j_c^2 \times t_1 \approx 0.55[(\pi^4 \rho \lambda)/\Omega_0] \qquad (1)$$

Here, j_c is the current density of the emitter (before its destruction) in units of A/cm^2; t_1 is the breakdown delay time in seconds; and ρ, λ, and Ω_0 are the density, thermal conductivity, and resistivity of the material, respectively.

Because of the huge difference in resistivity between metal and insulator, of the order of a dozen orders of magnitude, t_1 for velvet is very short. This is the reason why the velvet cathode has a very short "closure time."

Another unique feature of the velvet cathode is that its plasma moves at a very slow speed. Theoretically, the velocity of the metal-cathode plasma can be treated as a gas kinetics problem dealing with adiabatic diffusion of gas into vacuum. The velocity can be expressed as follows:

$$v = \{[4\gamma/(\gamma - 1)] \times \eta \times E\}^{1/2} \quad (2)$$

where $\gamma = c_p.c_v$ which is the adiabatic coefficient, E is the latent heat of sublimation for the metal, and η is the overheat coefficient. Since the velvet cathode plasma temperature is lower than that of a metal cathode, the velvet cathode plasma moves at a much lower velocity than that of a metal cathode.

How are electrons replenished from the metal substrate to the tips of the velvet cathode? There is a surface internal network theory. First, there are field-effect electrons in the high-field region near the metal-vacuum insulator interface. Then, these primary electrons bombard the surface of the insulator to create secondary electrons. Under the influence of the external field, electrons hop along the surface of the insulator to form a network on the velvet surface. Electrons are replenished to the tips by this mechanism. A detailed description of this mechanism is available in reference [9].

Recently, R.V. Latham, et al., presented an FIHEE (field-induced hot electron emission) model[6,7,8] to explain the prebreakdown electron emission mechanism on the high-voltage vacuum-insulator electrode surface. We believe that it might be used to explain the emission mechanism for the velvet cathode with short pulses (3 ns).

With an applied field between the anode and cathode, velvet is an excellent dielectric material. Hence, the external field could penetrate the velvet and reach the metal substrate to cause the energy levels to change.

There is a critical field in an insulator, approximately 10^5~10^6V/cm. When the applied field exceeds this strength, electrons can tunnel from the metal substrate to the conduction band of the velvet. This heats the velvet up and accelerates the ionization process which causes an avalanche in the conduction band of the velvet.

Let us assume that ΔV is the voltage drop across the velvet fiber, V is the applied voltage between the anode and cathode, d is the distance between the two electrodes, Δd is the thickness of the velvet and ϵ is the relative dielectric constant of the velvet, then

$$\Delta V \approx \left(\frac{1}{\epsilon}\right)\left(\frac{\Delta d}{d}\right) V \quad (3)$$

In our experiment, $\epsilon \approx 4$, V = 300~600 kV, d = 8 mm, Δd = 1.5 mm. Here, ΔV = 15~30 kV, and E = 10^5~2 x 10^5V/cm. Under such conditions, dielectric materials such as velvet have some conductive paths to convert the velvet from a nonconductive to a conductive state.

In the presence of a high field, the Poolo-Frenkel effect plays a major role (i.e., the field enhances thermal ionization between donors and traps). Then, the overall conductivity is a function of the applied field. In this case, J and ΔV may be expressed as follows:

$$\left.\begin{aligned} J &= J_o \exp\left[(e/kT)\,(e\Delta V/\varepsilon\varepsilon_0 d)^{1/2}\right] \\ \text{or}\quad J &= J_0 \exp\left[(e/2kT)\,(e\Delta V/\varepsilon\varepsilon_0 d)^{1/2}\right] \end{aligned}\right\} \qquad (4)$$

depending upon the location and characteristics of the trap.

In the short-pulse experiment, voltage and current profiles were measured after 30, 80, and 170 runs. From equation (3), we have the $(\Delta V)^{1/2}$ versus lnI curve (Figure 7). The results are in good agreement with the theory described above.

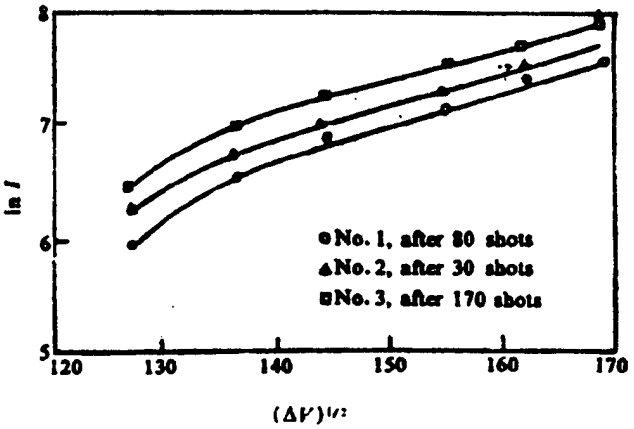

Figure 7. The Experimental Characteristics of lnI Versus $(\Delta V)^{1/2}$ of Velvet Cathode

In this case, the current density across the velvet is very high (approximately 7 kA/cm^2); therefore, some fibers are burnt. However, the entire pulse lasts a very short time and burning might have occurred at the late stage of emission.

Acknowledgement

This work was supported by the Japan Society for the Promotion of Science. The authors also wish to thank all the people at the Institute for Laser Science, University of Electro-Communications in Tokyo for their beneficial discussions and technical assistance.

References

1. R.J. Adler, G.F. Kiuttu, B.E. Simpkins, D.J. Sullivan, and D.E. Voss, AD-A149, 1984, p 250 and REV. SCI. INSTRUM., Vol 56 No 5, May 1985.

2. R.D. Scarpetti, D.A. Goerz, P.R. Bowen, R.L. Hodgin, and K.C. Wong, "Digest of Technical Papers, 6th IEEE Pulsed Power Conference," 1987, pp 631-634.

3. Ken-ichi Ueda and Hiroshi Takuma, "Advance Program of 11th Conference on Optical Fiber Communication and 5th International Conference on Optical Fiber Sensors," 1988, p 38.

4. R.K. Parker, R.E. Anderson, and C.V. Duncan, J. APPL. PHYS., Vol 45 No 6, Jun 1974.

5. G.A. Mesyats, E.A. Litvinov, and D.I. Proskurovsky, "Proceedings of the 4th International Symposium on Discharges and Electrical Insulation in Vacuum," Waterloo, Ontario, Canada, 1970, pp 82–95.

6. R.V. Latham, IEEE TRANS. ON ELECTRICAL INSULATION, Vol 23 No 5, 1988, pp 881–894.

7. K.H. Bayliss and R.V. Latham, PROCEEDINGS OF ROY. SOC. LOND., Vol A403, 1986, pp 285–311.

8. R.V. Latham, VACUUM, Vol 32 No 3, 1982, pp 137–140.

9. Takahiro Miura, et al., "Characteristics of Velvet Cathode for Electron-Beam-Excited KrF Laser," DIGEST OF TECHNICAL PAPERS, 10th Annual Meeting of the Laser Society of Japan, 1990, p 77.

Theoretical Analysis of Dual-REB Microwave Generators

92FE0442G Chengdu QIANG JIGUANG YU LIZI SHU [HIGH POWER LASER AND PARTICLE BEAMS] in Chinese Vol 4 No 1, Feb 92 pp 127-130

[Article by Li Chuanlu [2621 0278 5251], Liu Yonggui [0491 3057 6311], Qian Baoliang [6929 1405 5328], and Cheng Kaijia [4453 7030 3946] of the Department of Applied Physics, National University of Defense Technology, Changsha, Hunan 410073: "Theoretical Analysis of Dual-REB Microwave Generators"; MS received 28 Dec 90, revised 27 Apr 91]

[Text] **Abstract**

The physical mechanism of microwaves excited by two relativistic electron beams (REBs) in a cylindrical waveguide is studied based on magnetic-fluid theory. A dispersion relation has been derived in the presence of an infinite axial guiding magnetic field. An expression for the growth has also been found at the Cerenkov resonant point,[1] i.e., $\omega = kv_{\alpha 0}$. The dependence of growth rate upon related parameters is also briefly discussed.

I. Introduction

There are several types of high-power microwave generators,[2] such as the dielectric Cerenkov microwave generator, virtual cathode oscillator (vircator) microwave generator, and beam-plasma interaction microwave generator. Each type of microwave generator has its own unique advantages and limitations in terms of band, power, and structure.

A novel microwave generator, i.e., a dual-REB microwave generator, is presented in this paper. Physically speaking, when two electron beams move toward each other, they produce a two-stream instability.[3] If the two beams are placed in a cylindrical waveguide, this instability can be coupled to yield waveguide electromagnetic modes to consequently generate a microwave output. Since the parameters of the two electron beams can be adjusted, it is easy to achieve resonance.

II. Basic Equations

Assume the initial velocities of the two cold REBs are $\mathbf{v}_{\alpha 0} = v_{\alpha 0}\mathbf{e}_z$ and $\mathbf{v}_{\beta 0} = -v_{\beta 0}\mathbf{e}_z$, respectively. The two beams are distinguished by subscripts α and β. The continuity equation is:

$$\frac{\partial n_i}{\partial t} + \nabla \cdot (n_i v_i) = 0, \quad (i = \alpha, \beta) \tag{1}$$

The conservation of momentum equation is

$$\frac{d\boldsymbol{P}_i}{dt} = -e(\boldsymbol{E} + \frac{1}{c} v_i \times \boldsymbol{B}), \quad (i = \alpha, \beta) \tag{2}$$

where $\mathbf{P}_i = m\gamma_i \mathbf{v}_i$ represents the momentum of the electron; m, $\mathbf{v}_i$, and $-e$ are the electron mass, velocity, and charge, respectively; c is the speed of light in vacuum; n_i is the electron density, and $\gamma_i = (1 - v_i^2/c^2)^{-1/2}$ is the relativistic factor of the electron. $\mathbf{E}$ and $\mathbf{B}$ represent the electric and magnetic fields, respectively, and satisfy the Maxwell wave equation

$$(\nabla^2 - \frac{1}{c^2}\frac{\partial^2}{\partial t^2})\boldsymbol{E} = \frac{4\pi}{c^2}\frac{\partial \boldsymbol{J}}{\partial t} + \nabla(\nabla \cdot \boldsymbol{E}) \tag{3}$$

where $\boldsymbol{J} = \sum_i (-e\mathbf{v}_i n_i)$ is the total current density.

Equations (1), (2), and (3) are the basic equations of the magnetic-fluid model.

III. Dispersion Relation

When an infinitely large axial guiding magnetic field is applied to a cylindrical waveguide, the two REBs only move in one-dimension along $\mathbf{e}_z$. Let us assume that the two REBs have the same radius r_b, and the radius of the waveguide is R, the mean densities of the two beams are $n_{\alpha 0}$ and $n_{\beta 0}$, respectively. The dispersion relation may be derived from perturbation. To this end, we assume that

$$v_i = v_{i0} + v_{i1}, \quad n_i = n_{i0} + n_{i1}, \quad \mathbf{E} = \mathbf{E}_1, \quad \mathbf{B} = \mathbf{B}_1 \tag{4}$$

and

$$(v_{i1}, n_{i1}, \mathbf{E}_1, \mathbf{B}_1) \propto e^{i(kz-\omega t)} \tag{5}$$

where the subscript "1" represents a first-order perturbation term, and ω and k are the angular frequency of the electromagnetic wave and wave number along $\mathbf{e}_z$, respectively.

The two REBs in one-dimensional motion inside a cylindrical waveguide can only interact with the TM_{0n} mode, under the following boundary conditions:

$$E_z|_{r=R} = 0, \quad E_z|_{r=r_b^+} = E_z|_{r=r_b^-}, \quad \frac{\partial E_z}{\partial r}|_{r=r_b^+} = \frac{\partial E_z}{\partial r}|_{r=r_b^-} \tag{6}$$

The following dispersion equation can be derived from equations (1)~(3):

$$\frac{Y_0(pR)\,J_0'(pr_b) - J_0(pR)\,Y_0'(pr_b)}{Y_0(pR)\,J_0(pr_b) - J_0(pR)\,Y_0(pr_b)} = \frac{k_\perp}{p}\,\frac{J_0'(k_\perp r_b)}{J_0(k_\perp r_b)} \tag{7}$$

where

$$k_\perp^2 = [1 - \frac{\omega_{p\alpha}^2}{\gamma_{\alpha 0}^3 (kv_{\alpha 0}-\omega)^2} - \frac{\omega_{p\beta}^2}{\gamma_{\beta 0}^3 (kv_{\beta 0}+\omega)^2}]\, p^2 \tag{8}$$

$$p^2 = \frac{\omega^2}{c^2} - k^2 \tag{9}$$

J_0 and Y_0 represent the zeroth-order Bessel function of the first and second kind, respectively. In equation (8)

$$\omega_{pi} = (\frac{4\pi e^2 n_{i0}}{m})^{1/2}, \quad \gamma_{i0} = (1 - \frac{v_{i0}^2}{c^2})^{-1/2}, \quad i = \alpha, \beta$$

IV. Growth Rate of Instability

The dispersion equation (7) may be solved numerically. Let λ_{0n}/R be the nth root ($n = 1,2\cdots$) of $k_\perp$ in equation (7). When $R = r_b$, λ_{0n} is the root of $J_0(\lambda_{0n}) = 0$. Hence, from equation (8), we have

$$[1 - \frac{\omega_{p\alpha}^2}{\gamma_{\alpha 0}^3 (\omega-kv_{\alpha 0})^2} - \frac{\omega_{p\beta}^2}{\gamma_{\beta 0}^3 (\omega+kv_{\beta 0})^2}]\,(\omega^2 - k^2c^2) = \frac{\lambda_{0n}^2 c^2}{R^2} \tag{10}$$

Equation (10) clearly points out that the physical process in a dual-REB microwave generator is the process that leads to the coupling of the electromagnetic mode of the waveguide due to two-stream instability.

If both beams have similar electron velocities and densities, it is possible to find the growth rate of the pure growth mode where the real part of the frequency is close to zero from equation (10). Since the frequency is near zero, this mode is of no interest to us. Hence, let us consider the following situation where the density of electron beam α is much smaller than that of electron beam β, i.e.,

$$\frac{\omega_{p\alpha}^2}{\gamma_{\alpha 0}^3} \ll \frac{\omega_{p\beta}^2}{\gamma_{\beta 0}^3} \tag{11}$$

Near the Cerenkov resonant point $\omega = kv_{\alpha 0}$, because there might be some strong interaction between the electromagnetic wave and electron beam α, the maximum growth rate of instability can be obtained from equation (10).

$$\Gamma = \frac{\sqrt{3}}{2^{4/3}\gamma_{\alpha 0}} \left\{ \frac{\omega_{p\alpha}^2 \left(\frac{V_{\alpha 0}+V_{\beta 0}}{V_{\alpha 0}}\right)}{\omega_0^2 + \frac{\lambda_{0n}^2 C^2}{R^2}(\gamma_{\alpha 0}^2-1)\left[(\gamma_{\alpha 0}^2-1)\left(1+\frac{V_{\beta 0}}{V_{\alpha 0}}\right)+1\right]} \right\}^{1/3} \cdot \omega_0 \qquad (12)$$

where

$$\omega_0 = \left(\frac{\omega_{p\beta}^2}{\gamma_{\beta 0}^3 \left(1+\frac{V_{\beta 0}}{V_{\alpha 0}}\right)^2} - \frac{\lambda_{0n}^2 \gamma_{\alpha 0}^2 V_{\alpha 0}^2}{R^2} \right)^{1/2} \qquad (13)$$

The frequency of the microwave is

$$\omega = \omega_0 - \Gamma/\sqrt{3} \approx \omega_0 \qquad (14)$$

V. Conclusions

A magnetic-fluid model is used to study the interaction between two electron beams and a waveguide. Under the approximation that the densities of the two electron beams differ significantly, an expression, equation (12), for the maximum growth rate near the Cerenkov resonant point, $\omega \approx kv_{\alpha 0}$, is obtained. The results indicate that:

(1) The output microwave frequency is a function of $v_{\alpha 0}$, $v_{\beta 0}$, $n_{\alpha 0}$, $n_{\beta 0}$, R and r_b. By properly adjusting some parameters while keeping others unchanged, it is possible to achieve some degree of resonance. It might be more effective to adjust the electron density $n_{\beta 0}$ of REB β and the electron velocity $v_{\alpha 0}$ of REB α.

(2) The growth rate can be increased by raising the $n_{\alpha 0}$ and $n_{\beta 0}$ of the REBs.

(3) The growth rate can be lowered by increasing the velocity, or energy, of the REBs.

(4) With $\frac{\omega_{p\beta}^2}{\gamma_{\beta 0}^3 \left(1+\frac{V_{\beta 0}}{V_{\alpha 0}}\right)^2} > \frac{\lambda_{0n}^2 \gamma_{\alpha 0}^2 V_{\alpha 0}^2}{R^2}$ when n increases, λ_{0n} goes up and the growth rate of instability falls. Therefore, the growth rate of the lowest-order mode TM_{01} should be the highest.

(5) In order to illustrate that the electromagnetic radiation emitted by the dual-REB microwave generator is in the microwave range, a numerical example is given below.

Assume REB α and REB β have the same velocity, i.e., $\gamma_{\alpha 0} = \gamma_{\beta 0} = 1.196$ and $v_{\alpha 0} = v_{\beta 0} = 0.548c$. However, the densities are quite different: $n_{\alpha 0} = 2.688 \times 10^{11} cm^{-3}$ and $n_{\beta 0} = 4.30 \times 10^{12} cm^{-3}$. The radius of the cylindrical waveguide R = 1.5 cm. The electron beams almost fill the waveguide ($r_b \sim R$). From eq. (13) we can calculate that $\omega_0 = 3.178 \times 10^{10} s^{-1}$. From $\omega_0 = (2\pi/\lambda)v_{\alpha 0}$, the wavelength of the electromagnetic wave was calculated to be 3.248 cm.

Acknowledgement

This work is a part of the National Natural Science Foundation (NSFC) grant No. 8188108. The authors wish to express their sincere gratitude to the Chinese Society of Plasma Physics Research.

References

1. A.A. Galeev and R.N. Sudan, Basic Plasma Physics I, North-Holland Pub. Co., 1983, p 252.

2. V.L. Granatstein and I. Alexeff, "High-Power Microwave Sources," Artech House, 1987.

3. N.A. Clare and A.W. Televalepiece, "Principles of Plasma Physics," Atomic Energy Publ. House, 1983, p 142.

- END -